4

Emission of semiconductor nanocrystals in photonic crystal environment

Sergei G. Romanov* and Ulf Peschel
Cluster of Excellence "Advanced Engineered Materials"
Institute of Optics, Information and Photonics, University of Erlangen - Nürnberg, Günther-Scharowsky-Str.1, 91058 Erlangen, Germany
**Ioffe Physical Technical Institute, Polytekhnishesckaya ul., 26, 194021 St. Petersburg, Russia*

1. Introduction

Widespread application of colloidal semiconductor nanocrystals (NCs) [1] in light emitting devices is guaranteed by their low production cost, broadly variable emission frequency and relatively long lifetime. In order to exploit the advantages of NCs, the light sources should be equipped with non-dissipative photon management structures with the aim to form the spectrum of the source, to manage the emission diagram and to arrange the radiative recombination of electron excitations in the most purpose-efficient way. Obviously, the electrically biased light sources are the most application relevant [2], but developing the principles of photon management architectures can be performed with systems operating with photoexcitation of the NC emission.

One of the most awaiting realisations of the photon management in light sources is based on the photonic crystals (PhC). The radiation in such sources is controlled through modification of the electromagnetic vacuum [3,4,5]. The pre-condition of such control is the modulation of the photon density of states (DOS) that allows either accelerate or suppress the radiation rate of light emitters in a pre-defined spectral range. The development of PhC-based sources begun with investigation of the spectra and directionality changes of the emission from embedded sources. Nowadays the main aim is to design special defect states that are capable of purposive shaping the emission characteristics.

In PhC-based devices the emitter should be coupled to the outside world only via PhC eigenmodes in order to gain a full control upon emission characteristics. This can be achieved by immersing the emitter in the PhC interior. At the early stage it became clear that the fabrication of the 3-dimensional PhCs for the visible range of the spectrum took a long time due to complexity of required nanofabrication [6,7,8]. Meanwhile the nature offers an easy affordable solution – the opal crystals [9,10], the play of colours of which is based on principles of PhCs. Opals consist of face centred cubic packed lattice of silica spheres [11], i.e., the dielectric permittivity inside the opal is periodically modulated in all three dimensions. The interference of light waves that are scattered in the opal lattice results then in formation of directions, which are forbidden for propagation, if the wavelength is comparable to the lattice constant.

This phenomenon can be formalised in terms of the photonic energy band structure that looks similar to the electron energy band structure of solids. This energy band structure represents the dispersion of propagating modes in the energy-wavevector space. The spectral intervals without propagating modes are called the photonic bandgaps (PBG). Obviously, the complete absence of modes can be achieved only in infinitely large PhC with high refractive index contrast between scatterers and surrounding medium, hence, in reality it is more important to differentiate PhCs with omnidirectional and directional PBG. So far, no omnidirectional PBG was demonstrated in the visible due to the absence of dielectrics with high enough index of refraction [12], but this requirement can be fulfilled in the near-infrared with, e.g., Si or Ge-based inverted opals.

In the visible we ought to deal with directional bandgap crystals. This means that the internal light source, the emission of which is simultaneously coupled to the all available modes of a PhC, will not be blocked completely at any single frequency. Thus, there are two fractions of the energy flow – the one that is modified by the interaction with the structure and the other that leaks unaffected from the crystal. The aim of designing the photon management architectures is to tailor the fraction under control in the purposive way and to maximise the modified fraction of light flow.

The attractiveness of opals for emission manipulation was immediately realised by researches and the very first publications that considered the opal as a PhC were aimed primarily at the emission modification [13,14]. Certainly, the bulk opals in use were structurally very imperfect and the in-void synthesised emitters were randomly distributed over the PhC volume. However, even in such conditions it became possible to establish some links between PBG and emission characteristics. Since that time the tremendous progress was achieved triggered by the invention of artificial opal films of high structural quality [15]. Another crucial development in late 90s was the infiltration of the opals with colloidal NCs as a method that allows to preserve the crystal quality and the refractive index contrast of the opal-based PhC [16]. Nowadays semiconductor NCs are conveniently used in studies of the PhC light sources [17].

The opals discussed in this chapter are the PhC with the directional PBG. We will consider the photoluminescence (PL) from opal-embedded NCs possessing the emission band in the visible under continuous wave (cw) excitation of moderate power. Any time-resolved characteristics and optical non-linearities are outside the scope of our discussion. The aim of this chapter is to demonstrate what kind of emission modification one can achieve with NC that are evenly distributed over the opal-based PhC volume or placed in close vicinity to the PhC surface. We will describe several tests that allow to identify the emission changes and estimate the order of magnitude of these changes.

2. General properties of light sources in photonic crystals

Let us introduce some definitions. In the free space the number of electromagnetic (EM) field modes with frequency $\omega < \omega_0$ is $N(\omega) = \frac{\omega^3 V}{3\pi^2 c^3}$. Correspondingly, the mode density is $D(\omega) = \frac{dN(\omega)}{d\omega}$ and $D(\omega) \propto \omega^2$ (Fig.1). The dipole emission power is $U = \frac{4\pi^2\omega^3}{3V}\left|\vec{d}\right|^2 D(\omega)$ and the emission rate is $\Gamma = U/\hbar\omega \propto \omega D(\omega)$. Using the Golden Fermi rule and following [18]

we consider the 2-level system with the transition frequency ω_0 that interacts with EM field of vacuum. The rate of radiative recombination from an excited $|e\rangle$ to a ground $|g\rangle$ state can be written taking into account the field quantization as

$$\Gamma_{e\to g} = \frac{2\pi}{\hbar^2}\sum_{\vec{k},n}\left|\left\langle g,1_{\vec{k}n}\left|\hat{\vec{d}}\bullet\hat{\vec{E}}(\vec{x}_0)\right|e,vac\right\rangle\right|^2 \delta(\omega_{\vec{k},n}-\omega_0) \tag{0.1}$$

The summation is taken over all one photon states $\left|1_{\vec{k},n}\right\rangle$ that satisfy the energy conservation law. 2-level atom is located at x_0 and its dipole operator is $\hat{\vec{d}}$.

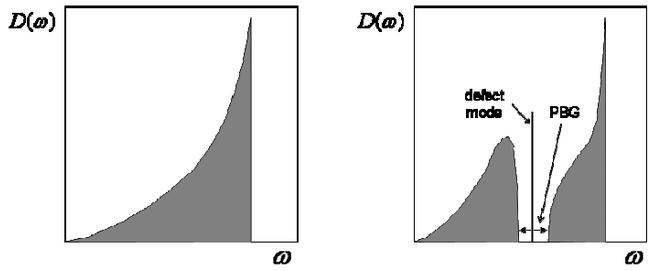

Fig. 1. (a) The spectrum of the optical mode density in a free space. (b) The same spectrum in a PhC with complete omnidirectional PBG. The defect mode is shown at the mid-frequency of the bandgap.

In the PhC this general expression is reduced to the density of modes $D(\omega)$. Let us expand the operator of electric field over the Bloch modes $\vec{E}_{\vec{k},n}(\vec{x})$ with quasimomentum $\vec{k}$ and number n.

$$\hat{\vec{E}}(\vec{x}) = \sum_{\vec{k},n}\sqrt{\frac{\hbar\omega_{\vec{k},n}}{2\varepsilon_0 V}}(\vec{E}_{\vec{k},n}(\vec{x})\hat{a}_{\vec{k},n} + h.c.) \tag{0.2}$$

where $\hat{a}_{\vec{k},n}$ - is the photon annihilation operator in the mode $\vec{k},n$, and the mode field is normalised to crystal volume

$$\frac{1}{V}\int_V dx\varepsilon(\vec{x})\left|\vec{E}_{\vec{k}.n}(\vec{x})\right|^2 = 1 \tag{0.3}$$

Then the emission rate is

$$\Gamma_{e\to g} = \frac{\pi\omega_0\left|\vec{d}\right|^2}{\varepsilon_0\hbar}\rho(\vec{x}_0,\vec{u},\omega_0) \tag{0.4}$$

where $\rho(\vec{x}_0,\vec{u},\omega_0)$ - is the projection of the local density of states (LDOS).

$$\rho(\vec{x}_0,\vec{u},\omega_0) = \frac{1}{V}\sum_{\vec{k},n}\left|\vec{u}\bullet\vec{E}_{\vec{k},n}(\vec{x}_0)\right|^2\delta(\omega_{\vec{k},n}-\omega_0), \tag{0.5}$$

where the matrix element of dipole transition $\vec{d} = \left\langle g \left| \hat{\vec{d}} \right| e \right\rangle$ and $\vec{u}$ is the unit vector along $\vec{d}$ direction. It is apparent from (0.4) that the photon emission rate is proportional to the density of photonic modes and the square of the electric field, in particular, the spontaneous emission is suppressed in the interval of low mode density. The full density of modes is the the local density of radiating states that is averaged over the dipole orientation in the unit cell. This is why the PBG in a full DOS $D(\omega) = 2\omega \sum_{\vec{k},n} \delta(\omega^2 - \omega_{\vec{k},n}^2)$ leads to the PBG in the local DOS independently on the emitter orientation.

LDOS differs from DOS by taking into account the distribution of the mode intensity in the primitive lattice cell [19]. In fact, the dipole can add a photon to the emission flux if not only the state is available in the field but also the field magnitude differs from zero in the dipole site. Depending on the dipole positioning in the unit cell of a PhC the LDOS changes and, accordingly, changes the emission rate. For example, the air modes at the upper PBG edge possess the field maximum in the regions of "light" dielectric. Hence, in order to maximise the outcome, the emitter should be positioned in the middle of the PhC voids. If this emitter finds itself in the point of the zero LDOS, only the weak spontaneous emission will be possible even in the non-zero total DOS. At the PBG edges the spontaneous emission can be enhanced, because of higher LDOS. But in the infinitely large PhC obeying the spherical symmetry (the case that cannot be realised experimentally) the Fermi Golden rule fails because of the DOS discontinuity. In the case of finite size PhC such discontinuity is replaced by van Hove singularity and disappears in the case of directional PBG.

In order to consider the stimulated emission one has to introduce the impurity atoms with certain volume density $\sigma(\vec{r})$ that experience the polarization α by the PhC field and possess the inverse population of their energy levels $\mathrm{Im}\,\alpha < 0$. Polarization of impurity atoms that is excited in point $(\vec{r},t)$ by the mode $E_{\vec{k},n}^{(T)}$ can be expressed as

$$P_{st}^{(1)}(\vec{r},t) = \alpha\sigma(\vec{r})E_{\vec{k},n}^{(T)}(\vec{r})\exp(-i\omega^{(T)}{}_{\vec{k},n} + \delta)t \tag{0.6}$$

In self consisted approach it is necessary to include the polarization wave $\vec{P}_{st}^{(2)}(\vec{r},t)$ that is induced by the field $\vec{E}^{(1)}(\vec{r},t)$:

$$\vec{P}_{st}^{(2)}(\vec{r},t) = \alpha\sigma(\vec{r})\vec{E}^{(1)}(\vec{r},t) \tag{0.7}$$

The polarization $\vec{P}_{st}^{(2)}(\vec{r},t)$ induces the electric wave

$$\vec{E}^{(2)}(\vec{r},t) = \tfrac{1}{2}\beta_{\vec{k},n}^2 l^2 \vec{E}_{\vec{k},n}^{(T)}\exp(-i\omega + \delta)t \quad (0.8) \tag{0.9}$$

the full self consisted stimulated field is expanded in the series

$$E_{\vec{k},n}^{(T)}(\vec{r}) = \sum_{j=0} \vec{E}^{(j)}(\vec{r},t) = \vec{E}_{\vec{k},n}^{(T)}(\vec{r})\exp(\beta_{\vec{k},n} l - (i\omega_{\vec{k},n}^{(T)} + \delta)t) \tag{0.10}$$

On the one hand, the enhancement factor of stimulated emission per unit length $\beta_{\vec{k},n} \propto 1/v_g(\vec{k},n)$ is inversely proportional to the group velocity $v_g(\vec{k},n) = \dfrac{\partial \omega_{\vec{k},n}^{(T)}}{\partial k_z}$ along, e.g., the z direction. On the other hand, $\beta_{\vec{k},n} = \dfrac{i\alpha\omega_{\vec{k},n}^{(T)} F_1(\vec{k},n)}{2v_g(\vec{k},n)}$, where the effective density of impurities normalised to the mode intensity $\vec{E}_{\vec{k},n}^{(T)}(\vec{r})$ is

$$F_1(\vec{k},n) = \frac{1}{V}\int_V \sigma(\vec{r})\left|\vec{E}_{\vec{k},n}^{(T)}(\vec{r})\right|^2 d\vec{r} \tag{0.11}$$

Finally, the stimulated emission $Est(\vec{r},t) = E_{\vec{k},n}^{(T)}(\vec{r})\exp(\beta_{\vec{k},n} l - (i\omega_{\vec{k},n}^{(T)} + \delta)t)$ acquires the enhancement in the range of slow waves.

It is worth noting the more elaborated approach to the dynamics of emission in PhC. For example, the strongest modification experiences the emitter whose emission band is located at the edge of the complete PBG due to strong DOS anomaly [20]. The emitter with transition frequency deeply inside PBG will emit photon, but this photon has no chance to propagate and will be absorbed by the same emitter. S. John named this situation as the „dressed" atom [21]. If the transition frequency falls close to the edge, the emission dynamics will be different from the free space emission owing to limited number of modes. This last case bears multiple quantum optics consequences, e.g. laser-like collective emission [22] due to non-Markovian interaction (the interaction that depends on its history) between the atom and the field.

In the case of directional PBG in finite size PhCs the effect of PBG upon the spontaneous emission becomes much less pronounced, first of all, because of the shallow variation of the DOS spectrum in the PBG [23]. Hence, such crystals can be used, primarily, to design PhCs with pre-defined emission indicatrix and for directional enhancement or suppression of the emission in a pre-defined spectral range.

For the inefficient light sources with low quantum efficiency $\eta << 1$, the overall relaxation rate

$$\Gamma_{tot} = \Gamma_{NR}(1 + \eta + \mathrm{O}(\eta^2)) \tag{0.12}$$

is defined by the non-radiative transitions Γ_{NR}. Then, the emitter power

$$I = P\Gamma_{rad}/\Gamma_{NR} \tag{0.13}$$

must be proportional the radiative emission rate and correspondingly, to the LDOS as well as the pumping power P. This case is applicable to all experiments described below. It should be emphasised that the power emitted in the narrow homogeneous emission band is proportional to LDOS only if the emission bandwidth is much narrower compared to the spectral interval of the LDOS variation. In the opposite case, namely the emitter with the broad inhomogeneous bandwidth, the LDOS spectrum should be acquired. One way to

obtain the LDOS spectrum is to compare the emission of two samples, one PhC-based and one non-PBG reference that possess the same channel of non-radiative recombination [24]:

$$\frac{I_{PhC}}{I_{ref}} = \frac{P_{PhC}}{P_{ref}} \times \frac{\Gamma_{radPhC}}{\Gamma_{rad.ref}} = K \frac{D_{radPhC}(\omega)}{D_{rad.ref}(\omega)} \tag{0.14}$$

This is the true spectrum only in the case of quadratic DOS spectrum in the reference sample and the emitter localisation in the PhC along the constant LDOS surface. In the opposite and more frequent case of the broad distribution of emitters over the unit cell volume, this method produces the correct estimate of specific extrema in LDOS spectrum.

3. Experimental technique

The opal crystals used for impregnation with colloidal NC are the thin film crystals prepared by either sedimentation or by crystallization in the moving meniscus. This technology is well established and documented [15]. The current improvement of crystallization methods aims at eliminating the cracks of the film [25] and better crystallinity [26]. Typical example of the opal film is shown in Fig.2. The symmetry of the opal lattice is very close to the face centred cubic (fcc) symmetry (Fig.3). Opal possess the open porosity that allows embedding the semiconductor NCs in voids between touching spheres (Fig.3a,b). In order to describe the light propagation in the PhC it is convenient to use the lattice representation in the reciprocal space (Fig.3c). If the optical data are collected along the normal to the opal film, this direction corresponds to the ΓL directions in the 1st Brillouin zone. The dashed line on the surface of the Brillouin zone is the line along which the data were obtained along the oblique direction to the film normal.

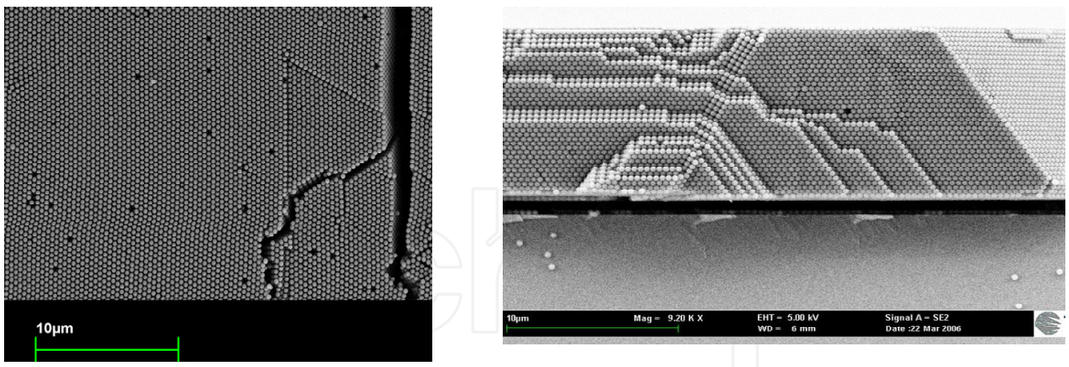

Fig. 2. Scanning electron microscope images. Top view (left panel) shows the (111) plane of fcc lattice at the film surface and the film cracks on the right hand side and side view (right) shows the film cross-section. The opal film is crystallised in the moving meniscus from PMMA spheres of 368 nm in diameter.

Transmission/reflectance spectra of the opal films were measured under white light illumination from a tungsten lamp. The transmitted/reflected light was collected within a solid angle of approximately 2° along different directions with respect to the [111] axis.

The energy band structure of the opal film was calculated under assumption of the fcc lattice symmetry (Fig.3d). This diagram relatively closely corresponds to the PBG structure revealed by the transmission spectra of the opal film measured at different angles of light propagation (Fig.3e). Bragg law approximation allows to associate the most pronounced resonances in these transmission spectra with diffraction at crystal planes.

PL measurements were performed under continuous wave (cw) excitation from an Ar+ gas laser (Fig.4). Typically, the beam was focused in 0.1 mm in diameter spot. Two schemes were used for PL excitation/collection – the back window, in which the PL is collected from the sample side that is opposite with respect to illuminated side, and the front window, in which the PL signal was measured from the same illuminated side of the sample (Fig.5). The PL was typically collected from a solid angle $\Omega = 5^o$. PL spectra were recorded, when the PL intensity becomes stable after each change of the excitation power. In order to trace the anisotropy of the emission, PL spectra were measured at different angles θ with respect to the [111] axis of the opal lattice. In the case of an array of randomly oriented dipoles smaller than the wavelength, the averaging over the sample volume results in an isotropic light source. In this case, the distortion of the spherical wavefront of an isotropic PhC-embedded emitter is a direct consequence of the PBG. In what follows, we will refer to the fraction of the wavefront that is blocked for propagation by the first bandgap as the Bragg cone.

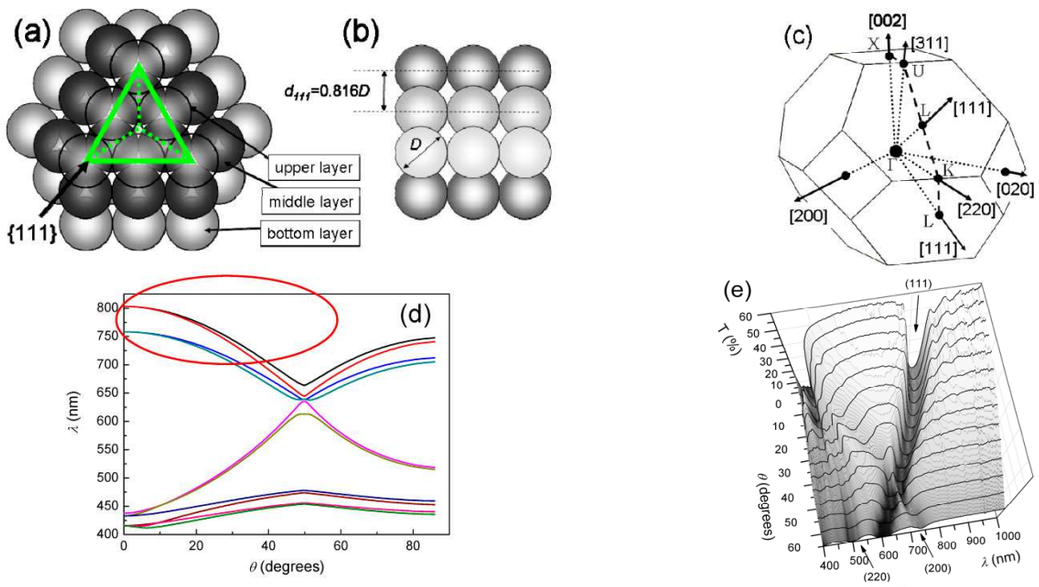

Fig. 3. (a, b) Schematics of the fcc lattice fragment. The {111} family of planes is represented by a tetrahedron. The interstitial voids between touching spheres are clearly seen. (c) Brillouin zone of the fcc lattice. Letters show the main symmetry points. Numbers at arrows name the directions in the reciprocal space in correspondence to the lattice axes in the real space. (d) The energy band structure of the opal crystal assembled from PMMA spheres of 368 nm in diameter (see Fig.2). The ellipse marks the typical range of this diagram, which is relevant to the discussion in this chapter. (e) Example of experimental transmission spectra of the opal film from 368 nm spheres measured under s-polarised light [27]. Numbers are the Miller indices of fcc crystal planes, the diffraction at which corresponds to the transmission minima (compare to panel (d)).

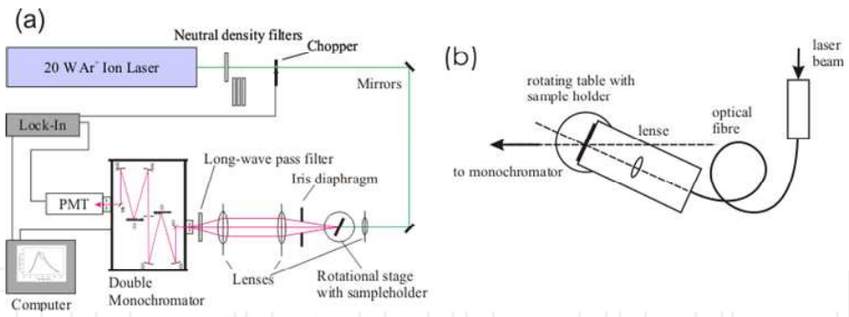

Fig. 4. (a) Schematics of the PL typical measurement set-up – cw excitation and lock-in-based registration detection. (b) Improved excitation conditions to allow constant size of illuminated spot to be preserved while changing the detection angle.

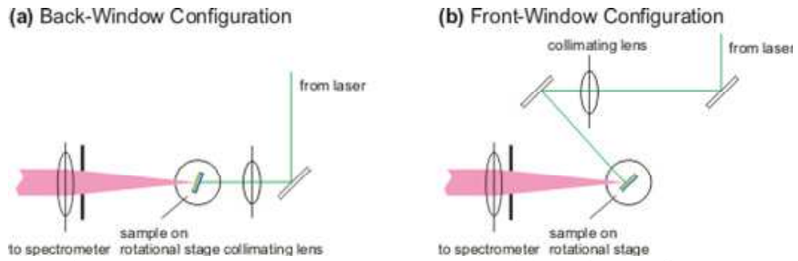

Fig. 5. Schematics of PL measurements in transmission (a) and in reflectance mode (b).

4. Directional suppression of CdTe nanocrystal emission in thin opal film

The opal films for this experiment were prepared from 1% aqueous colloidal solution of latex spheres of D=240 nm in diameter dried on glass slides (1 cm²). Films crystallize in the randomised fcc lattice, which has the [111] axis as the growth direction. Subsequently, films with a thickness of 20-30 μm were sintered for 2 h at 100°C. CdTe core-shell NCs were synthesized as described elsewhere [28]. A polymer shell was used to prevent the agglomeration of colloidal particles. Infiltration of CdTe colloidal NCs into an opal film was performed by dipping the latter in 0.02 M (referring to Te) CdTe NC aqueous colloidal suspension for 1 min. As a result of electrical charging of these polymer shells, the CdTe NCs are attached to the surface of latex spheres (Fig.6a).

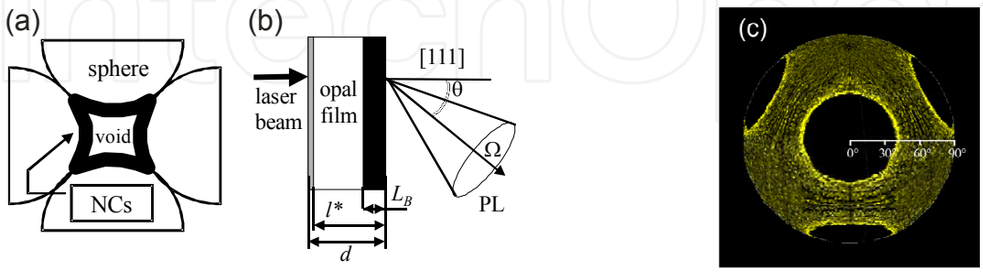

Fig. 6. (a) Schematics of NC CdTe layout in the octahedral opal void. (b) Characteristic length scales that are relevant to the formation of the emission spectrum of opal-embedded NC. (c) The spatial distribution of emission from a point source located inside the opal lattice. View along [111] axis ($\theta = 0^o$). Black holes are the Bragg cones. *Courtesy of D. Chigrin*.

The transmission spectrum of the opal film demonstrates the minimum centred at 2.23 eV (Fig.7a), which manifests the directional (111) bandgap. The position of this minimum corresponds to the Bragg diffraction resonance at the stack of (111) planes in the fcc lattice (Fig.3b) $\hbar\omega_B = 2\pi c/(2\times n_{eff}\times 0.816D)$, where n_{eff} is the effective index of refraction obtained from the effective medium approximation to the opal lattice and c is the light velocity. The relative bandwidth of the transmission minimum $\Delta E/E_B \approx 0.067$ exceeds by 20% the gapwidth calculated for ideally packed opal [29], which is an indication of lattice disorder. Impregnation of the opal with CdTe NCs leads to the "red" shift of this minimum by 0.05 eV due to increase of the refractive index and the transmission reduction at $\hbar\omega > 2.5$ eV, i.e., above the absorption edge of CdTe NCs. The CdTe fraction can be estimated from this shift as 1 to 2 volume % (for different samples) or up to 4% of the void volume. Important, that impregnating the opal with NCs does not destroy the optical quality of the opal-based PhC.
The spectral position of the transmission minimum changes rapidly with changing the incidence angle of the light beam with respect to the film normal according to the Bragg law. Due to the destructive influence of opal crystal defects the transmission attenuation in (111) resonance gradually decreases with the angle increase $\theta \geq 70^o$ (Fig.3e) [26].
The relatively narrow linewidth of the NC emission (Fig.7b) compared to the PBG width would not allow for tracing the emission change at different overlaps with the PBG. But the PL bandwidth of NC in the opal appears much broader due to NC interaction with the inner opal surface. Moreover, the PL bandwidth in the CdTe-opal was broadened due to partial degradation of the NC luminescence after intense laser light illumination. On a later stage the excitation power was kept below 6 mW to avoid further degradation of NC emission. The PL spectrum of CdTe-opal collected at θ = 70° represents the emission of CdTe NCs in the latex opal without influence of the directional PBG (Fig.7b).

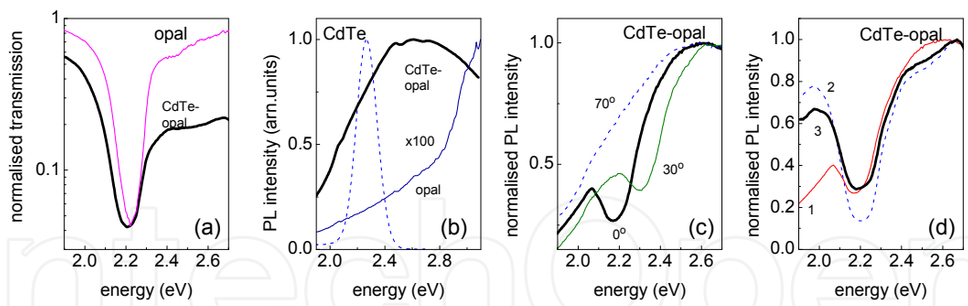

Fig. 7. (a) Transmission spectra at $\theta = 0^o$ of the latex opal assembled from spheres of $D = 240$ нм and the opal impregnated with NC CdTe. (b) PL spectrum of NC in water suspension (dashed line) in comparison to PL spectra of the bare opal (thin line) and CdTe-opal (thick line) obtained at $\theta = 70^o$ under excitation by 351 nm line of Ar+-laser with 1.9 mW power in a spot of 0.1 mm in diameter and collected from a 5° wide solid angle. The PL intensity of bare opal is >100 times weaker in magnitude compared to that of CdTe-opal. (c) PL spectra of CdTe-opal at different angles of collection. (d) Comparison of the CdTe-opal PL spectrum obtained at $\theta = 0^o$ (curve 1) and the reconstructed spectra obtained by multiplication the transmission spectrum and PL spectrum at $\theta = 70^o$ (2) and the same as (2) but with the account taken for the fraction of non-modified emission (3).

If the bandgap is present, the emission flow is PBG-blocked along the Bragg cones (Fig.6c) and the central frequency of the PL minimum coincides with the transmission dip. The angle dependence of PL spectra is clearly seen from comparison of spectra collected at $\theta = 0^o$ and 30^o (Fig.7c). This angle dispersion of PL minimum follows that of the transmission minimum. In particular, in the Brillouin zone, the $\theta = 30^o$ corresponds to the shift along the LU line from the ΓL towards ΓU direction (Fig.3c).

One can notice that the intensity contrast for the PL dip is reduced by a factor of two compared to the 6-fold reduction in the transmission minimum. To understand this we have to separate the measured emission flux in the ballistic and the diffuse components. The diffuse background is comprised by photons, which experience scattering at lattice defects [30]. In thin film opals the mean free path of photons, *l**, is about 15 μm that is shorter the film thickness (Fig.6b), i.e. scrambling of trajectories of photons emitted at the distance from the film edge *l*>*l** is expected at any detection angle. Moreover, the scattering results in progressively shallower dip at higher angles of detection due to the longer light path. Another source of unstructured emission is the near-surface emission that comes without attenuation and fills in the PBG minimum. In the bulk opals the latter contribution can be eliminated by bleaching the emitters in the near-surface zone [31], whereas in the thin film opals one can use the photonic hetero-crystal approach (see section 8).

The unstructured contribution to the PL spectrum can be quantitatively estimated using the spectrum of unmodified emission at $\theta = 70^o$ and the transmission spectrum at $\theta = 0^o$ [32]. The result of $I_{PL}(\theta = 0) = I_{PL}(70) \times T(0)$ is shown by curve 2 in Fig.7d, which overestimates the emission suppression. More accurate fit (curve 3) can be obtained taking into account the diffuse light $I_{PL}(\theta = 0) = 3I_{PL}(70) \times T(0) + 0.25I_{PL}(70)$. This consideration proves the substantial diffuse fraction in the light detected along the PBG direction.

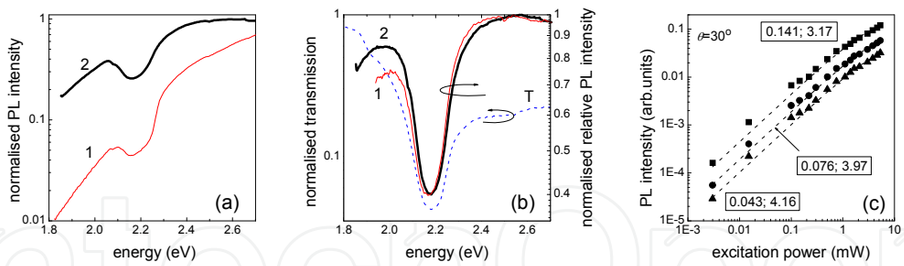

Fig. 8. (a) PL spectra of CdTe-opal with ~1 vol.% (1) and ~2 vol.% (2) CdTe fraction at $\theta = 0^o$. (b) Relative PL intensity spectra of CdTe-opal at low (1) and high (2) CdTe fraction in comparison to transmission spectrum. (c) Input-output characteristics of PL intensity acquired at $\theta = 30^o$ and $\hbar\omega = 2.5, 2.3$ and 2 eV (squares, circles and triangles, respectively). Points –experiment, lines – two-parametric approximation, numbers - fit parameters I_0 and P_0, respectively.

Next test was made to check if the NC-opal spectrum depends on the NC concentration. Obviously, only low volume concentration was explored, because with high fraction of NC the PBG properties of the samples will be altered dramatically due to changing the refractive index contrast and the uneven NC distribution over the opal voids. Fig.8a demonstrates the

almost 2-fold increase of the PL intensity followed the doubling of NC concentration. Moreover, the PBG attenuation in the relative PL spectrum remains almost the same (Fig.8b). It is worth noting that obtaining the relative PL spectrum, as it was suggested in early works [33,34], is the very useful method for revealing the PBG effect upon the emission of PhC-coupled light sources especially in the case of complex spectra and weak attenuations.

5. Stimulation of CdTe nanocrystal emission in thin opal film

In the case of an externally pumped emitter inside a PhC of finite size, the field of the photonic mode becomes a superposition of the outgoing waves and the waves reflected from the PhC boundary. For the PBG frequencies the light intensity decays exponentially with distance z into the photonic crystal. Such photonic mode has the form of a standing wave with an envelope function that decays exponentially as $\exp(-\gamma z)$, where γ is the extinction coefficient. Thus, this mode in an opal film is a standing wave formed by interfering evanescent Bloch states inside the crystal and a plane wave in the vacuum.

For a microscopic emitter in the PhC the amplitude of the external field will depend on the distance from the boundary of the PC and will be determined by (i) the strength of the light attenuation in the photonic crystal and (ii) the position of the emitter relative to the nodes and antinodes of the standing evanescent Bloch wave (LDOS). Note that attenuation of light always leads to a decrease of the field and also of the emission rate while the position of the emitter relative to the standing wave of the field can decrease (in the node) or increase (in the antinode) the emission rate. The experimental results show the intensity suppression in the PBG frequency range. As was shown, within the PBG the PL is composed of light emitted at different distances from the PhC boundary. It can be concluded from the transmission spectra that the attenuation length corresponding to the centre of the band gap is about 10 μm (6 μm for an ideal structure) [35]. Thus, only $\sim 1/3$ of the 30 μm thick opal film contributes to the PL intensity observed externally ($\sim 1/5$ for the ideal lattice). These estimates are in good agreement with the measured relative PL intensity, shown in Fig.7b, which exhibits a decrease of PL intensity by a factor of five.

The PL intensity of the NC-opal as a function of the excitation power can be represented by input-output characteristics (Fig.8c). These characteristics exhibit saturation with increasing excitation power for all explored frequencies and can be fitted to the expression

$$I_{PL} = I_0(1 - \exp(-P/P_0)), \tag{0.15}$$

where P is the excitation power. In this fit the pre-factor I_0 is the power radiated by a saturated emitter and the parameter P_0 in the emission saturation threshold. Since these parameters acquire unique values for a given frequency and angle of detection, they can be represented in a spectral form. The $I_0(\hbar\omega)$ spectrum at 70^o is a monotonous function of frequency (Fig.9c). It is measured in PL intensity units and closely resembles the PL spectrum. The parameter $P_0(\hbar\omega)$ is given in excitation power units and corresponds to the projected excitation leading to a complete saturation of the input-output curve.

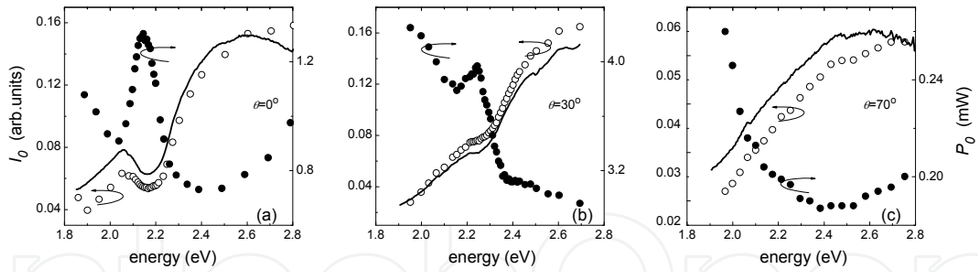

Fig. 9. Spectra of parameters I_0 (open circles) and P_0 (circles) at three detection angles $\theta = 0, 30, 70^o$. PL spectra are shown by lines for comparison.

The $I_0(\hbar\omega)$ spectra at θ = 0° and 30° follow the canvas for that at θ = 70° with the exception of the clearly resolved minimum superimposed on the monotonous background (Fig.8a,b). Moreover, $I_0(\hbar\omega)$ spectra closely resemble the PL spectra. By contrast, the spectra of the saturation threshold $P_0(\hbar\omega)$ at θ = 0° and 30° have their maxima in the bandgap. In particular, P_0 peak is located at the low frequency edge of the bandgap, covers the whole bandgap range and follows the bandgap angular dispersion. The P_0 magnitude is nearly doubled in the gap along the [111] axis, but its resolution becomes worse with increasing detection angle. Such degradation correlates the decrease of ballistic component in the detected emission flow because, neglecting mode re-coupling at the opal-air boundary, the emitter in the ballistic limit radiates in the same mode as detected outside the PhC.

Positioning of emitting NCs along the "heavy" dielectric boundary aligns them with the EM field distribution in the unit cell of the opal that ensures sampling by all NCs the same LDOS. In the case of a saturated emitter and in the presence of an effective non-radiative recombination channel, the radiated power is proportional to the spontaneous emission rate to a given mode (0.13). Therefore, the $I_0(\hbar\omega,\theta)$ is an estimate of the spontaneous emission rate spectrum along a given direction. The good correlation between $I_0(\hbar\omega)$ and the PL spectrum for a given direction (Fig.9) suggests that the spontaneous emission is the dominating process in the radiative relaxation in the opal-embedded NCs.

P_0 measures the range of the emission response to the pump power increase. For a given number of NCs, it depends on several factors. One is the probability of an electron transition between two bands in a NC band structure that is constant in this experiment. Another is the population of these bands. The others are the probability of coupling the emitted photon to the optical mode reservoir of the PhC and the balance between radiative and non-radiative relaxation. At θ = 70° the $P_0(\hbar\omega)$ is dominated by processes in the electronic system of the CdTe NCs (Fig.9c).

The weak variation of the saturation threshold across the emission band corresponds to a uniform density of electrons as a function of energy. Such distribution is the result of non-resonant excitation and fast non-radiative relaxation of the electronic excitations. The CdTe NCs in the opal suffer the surface effects that have an extremely strong influence on the electronic structure. In particular a wide "impurity" band is formed due to the surface states (which can be Tamm-like states, surface defects, and impurity atoms localized at the surfaces). Relaxation of electrons and holes within this large energy band has essentially a

hopping character [36,37,38], that provides quite a uniform energy distribution of carriers within the band. Roughly speaking, an electron jumps from one localized state to another with almost the same probability for the states of similar or markedly different energies. Due to Auger processes [39], which are extremely efficient near surfaces, the hopping relaxation is likely to happen. Thus the fact that there is similar character of the dependence of the PL intensity on the pumping for the frequencies below and above the PBG indicate that the energy distribution of carriers is almost pumping-independent in provided experimental conditions.

In turn, the sublinear character of the input-output characteristics suggests that the rate of non-radiative recombination grows super-linearly with the increase of carrier concentration n. This is typical for some processes, e.g., the Auger recombination rate is proportional to n^2 [39]. We can roughly estimate the influence of non-radiative recombination and variation of radiative lifetime on the dependence of PL intensity on pumping. Assuming for simplicity, that PL intensity is proportional to the carrier concentration n and can be characterized by "mean radiative lifetime" τ (the rate of radiative recombination is n/τ), we obtain that at the equilibrium $\partial n / \partial t = 0$ the excitation is equal to the relaxation

$$P = \frac{n}{\tau} + \Gamma_{NR}(n) \tag{0.16}$$

Within the PBG, the PL intensity is influenced by the increase of radiative lifetime τ. We may then ask how does such increase will modify the dependence of I on P in the system with spontaneous recombination and a super-linear dependence of $\Gamma_{NR}(n)$ on carrier concentration? Taking the derivative of the pumping P in eq. (0.16) with respect to the PL intensity I and noting that $I = n/\tau$, we obtain

$$\frac{\partial P}{\partial (n/\tau)} = 1 + \tau \frac{\partial \Gamma_{NR}}{\partial n} \quad \text{or} \quad \frac{\partial I}{\partial P} = \frac{1}{1 + \tau \dfrac{\partial \Gamma_{NR}}{\partial n}} \tag{0.17}$$

Taking into account that $\partial \Gamma_{NR}(n)/\partial n > 0$, we find that the increase of radiative lifetime τ leads to a slower growth of the PL intensity with increased pumping. In other words, the saturation threshold for a frequency within the PBG has to be less than that for a frequency outside the PBG. But this conclusion contradicts the observed PBG-related peak of $P_0(\hbar\omega)$ (Fig.9). To resolve this conflict one has to assume the presence of the amplified spontaneous emission in addition to the spontaneous one. The acceleration of the emission rate is a consequence of applying resonant conditions upon the emitter at a certain frequency. In what follows we will discuss two realizations of resonant modes in opal PhCs, bearing in mind that the modes of the allowed band are propagating ones, whereas the modes of the Bragg cone are the leakage modes of a PBG resonator. Nevertheless, since these resonance conditions are intrinsic to the PhC, we can postulate the omnipresence of the emission enhancement in the incomplete PBG.

5.1. Coupling to slow propagating modes

One source of the emission amplification in PhC can be associated with slowly propagating modes. The complex topology of iso-frequency surfaces in an incomplete PhC gives rise to beam steering effects [40,41,42]. As a result, the actual direction of the energy flow inside a PhC does not necessarily coincide with the mode wavevector $\boldsymbol{k}$, i.e., photons emitted with different wavevectors can propagate along the same direction. The iso-energy surface in k-space of the opal lattice in the PBG range contains eight necks, two per each [111] axis (Fig.6c, 10a) [43]. When this surface crosses the boundary of the 1st Brillouin zone (BZ), the normal component of the group velocity vector $\boldsymbol{v}$ vanishes. This means that all eigenmodes, the wavevectors of which end up at the intersection of the neck with the zone boundary, have the $\boldsymbol{v}$ pointing along the BZ boundary. Due to the topology of the 1st BZ, some eigenmodes with wavevectors along the $[\bar{1}11]$ direction and group velocity pointing in the [111] direction are expected. Because the direction of energy transport in a non-absorbing PhC coincides with the group velocity vector, there should always be some energy flux in the Bragg cone. In what follows, we will refer to modes with wavevectors parallel to the group velocity vector, as type 1 modes and to other modes as type 2 modes [44].

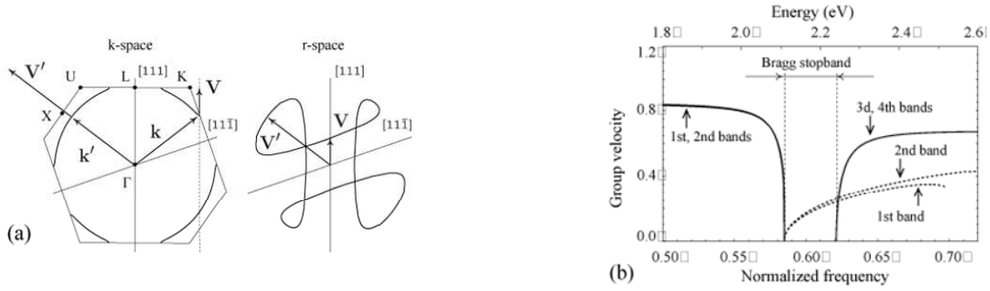

Fig. 10. (a) Iso-frequency (left) and group velocity (right) contours of opal at the frequency within the Bragg bandgap. $\boldsymbol{k}$ and $\boldsymbol{v}$ are vectors of type 2 inhomogeneous waves pointing along the [111] axis. (b) Group velocities of type 1 (solid curves) and type 2 (dash curves) Bloch modes along the [111] direction. The group velocity is given in units of c.

Fig. 10b shows the calculated group velocities along the [111] axis for wavevectors of the XULK section of the first Brillouin zone. Calculations were performed using the plane wave expansion method [45], where the Hellmann-Feynman theorem was used to calculate the group velocity vectors. The best fit to experimental data was obtained for the opal made of 243 nm diameter spheres of $n_{eff} = 1.6$. It is instructive to separate contributions to the energy flux from type 1 and type 2 eigenmodes. For frequencies below the Bragg bandgap, the flux along the [111] direction is solely formed by type 1 modes of the 1st and 2nd photonic bands. Within the PBG, only type 2 modes of the 1st and 2nd bands contribute to the flux. Above the PBG, the flux is composed by the type 1 modes of the 3d and 4th bands as well as by the type 2 modes of the 1st and 2nd bands. For sake of clarity, contributions of the latter are omitted in Fig. 10b, because their frequencies are above the Bragg gap.

The group velocity vanishes at the low frequency bandgap edge in the ballistic limit of an infinite PhC and then grows slowly with increasing frequency, comprising, in average, 1/10 of the group velocity absolute value outside a bandgap. Correspondingly, type 2 modes traverse the opal slowly and interact with the pumped medium for longer time. In agreement with this model, the slowing down of the group velocity towards the low

frequency bandedge is the reason for the "red" shift of the P_0-spectrum maximum with respect to the pseudogap centre (Fig. 9a).
The relative number of type 2 modes is proportional to the ratio of the small solid angle in *k*-space and the corresponding solid angle in real space:

$$N \sim \sum d\Omega_k / d\Omega \tag{0.18}$$

where the summation is taken over all contributions to the energy flux [43]. Since the type 2 modes originate at the necks of the dispersion surface, the ratio of the solid angles in (0.18) is below 4% over the bandgap. Correspondingly, the contribution of the stimulated emission to the total PL signal is small.

5.2. Coupling to defect modes

The available in the Bragg cone modes are the leakage modes of a PBG resonator. An obvious example of a resonator inside the opal is a lattice defect with its mode in the PBG. The quality factor of defect modes depends on the correlation between the localization length l_{loc} and the opal film thickness t, the distance to the opal boundary, the detuning of the resonant frequency from the PBG centre and the coupling of this resonance to similar defect modes. The radiation coupled to the eigenmode of a single defect is localized in the defect vicinity. In this case, the photon occupation number of this mode and the corresponding strength of the EM field increases under the cw pumping. Consequently, the radiated power acquires a super-linear component due to the backreaction of the emitted radiation upon the radiative transition probability. In the directional PBG, this effect also acquires the related anisotropy. In an opal with relatively high defect concentration, the defect modes are coupled throughout the film and the resulting quality factor is diminished.
It is instructive to demonstrate the presence of amplified spontaneous emission simply by plotting the ratio of PL spectra acquired at different excitation power. Such ratio spectra show a peak that corresponds to a dip in transmission spectra indicating that PL intensity grows faster with the increase of pumping inside PBG than outside. There is a shift of the maximum in the ratio spectra to higher photon energy with the detuning of angle of incidence from [111] (Fig.11).

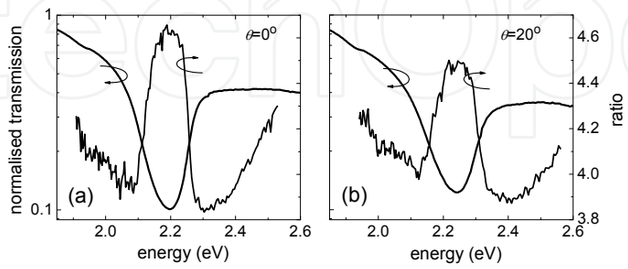

Fig. 11. The ratio of PL spectra acquired at excitation powers 2.54 and 0.49 mW vs. transmission spectrum at $\theta = 0$ and 20^o in panels (a) and (b), respectively. The measurements were performed at T=18K in order to reduce the non-radiative relaxation probability.

Faster growth of PL intensity inside the PBG is clearly seen also in Fig.12 (a, b). In Fig.12c one can see that in the PBG spectral range the PL intensity increases much faster with more intensive pumping than outside the PBG. Moreover, this effect gets stronger with the increase of the absolute value of pumping, and this indicates that the functions $I^{in}/I_{1,2}^{out}$ possess more complicated dependence on excitation power than a simple power law [35].

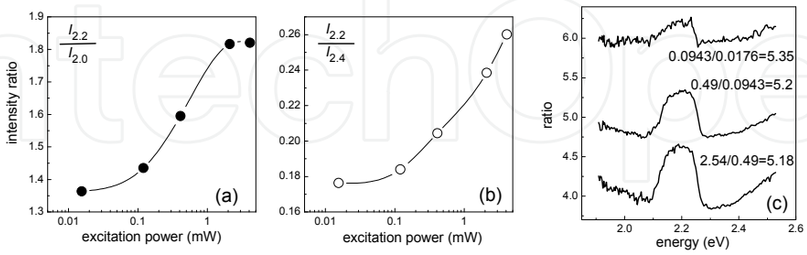

Fig. 12. Ratios of I^{in}/I_2^{out} and I^{in}/I_1^{out} at (a) frequencies $\hbar\omega = 2.2 \text{ and } 2.0 \text{ eV}$ and (b) at $2.2 \text{ and } 2.4 \text{ eV}$ as a function of pumping. (c) Ratios of the PL spectra along [111] direction obtained at different levels of pumping intensities: 0.943 and 0.0176 mW; 0.49 and 0. 0.943mW; 2.54 and 0.49 mW. The peak magnitude increases with increasing the power for the same power increment.

Thus apart from spontaneous emission, which is characterized by an increased radiative lifetime, there is a competing process that is characterized by faster dependence on *P* within the PBG. Let us check if the emission coupling into localized photon states of lattice defects which are located in the PBG can bring such effect. In disordered media a light wave can be localized due to multiple scattering [46,47], but such localization can be more easily achieved introducing disorder in otherwise periodic media [6]. In the latter case, the localization of light leads to the appearance of a non-zero density of photonic states in the PBG [48,49]. The localized modes, contrary to the evanescent modes, can have large electric field amplitude in the bulk of PhC, and, as a result, the radiative recombination time in such modes is much smaller. Consequently, the recombination is channelled into the localized modes which act as photon reservoirs. According to the Einstein principle, the radiative recombination in a single localized mode can be written as

$$I_{loc} = \frac{n}{\tau_{loc}} + s(P)\frac{n}{\tau_{loc}} \tag{0.19}$$

where τ_{loc} is the spontaneous radiative recombination time and *s* is the number of photons in the mode. The first and second terms in Eq.(0.19) is the spontaneous and stimulated emission, respectively. In the bulk homogeneous medium at moderate excitations (in case of lasers – below lasing threshold) the relation $s \ll 1$ holds, and therefore the stimulated emission can be neglected. In case of disordered PhC, the photon accumulation in the localized modes can lead to substantial enhancement of stimulated emission. It is obvious that the second term in Eq.(0.19) depends on the pumping power superlinearly. Thus, the experimentally observed increase of parameter P_0 or the peak in ratio of PL intensities at

different pumping intensities inside PBG can be explained by stimulated emission through the localized modes.

On the other hand, when a light-amplifying material is inserted into a PC, each localized state can be considered as the analogue of a laser mode. For laser modes the dependence of the PL intensity on the pumping has an abrupt change at threshold. Each laser mode is characterized by its own decay time (or Q-factor) and spatial distribution of the electromagnetic field. In the case of localized defect modes, the spatial distribution of the field can be altered by varying the pumping [50]. Therefore, the threshold intensity is different for different modes. One can conclude that the dependence of the PL intensity upon the pumping averaged over different modes should be some superlinear function, and could explain the faster growth of $I(P)$ within the PBG.

Another disorder-induced modification of the observed PL intensity is related to the scattering of the radiation in the localized mode into a propagating mode. Such a process makes possible the propagation of an emitted photon from the bulk of PhCs to the boundary without attenuation. Consequently, it leads to an increase in the effective thickness of the layer contributing to the detected PL intensity.

6. Emission indicatrix

The emission conditions for dipoles change as soon as the pseudogap overlaps with the emission band (Fig.13a). In the first approximation, the spatial pattern of emission changes according to the shift of the Bragg cone (Fig.6c). In the angle-resolved measurements, the PL intensity for the given direction is proportional to the part of the total radiated power, which is coupled to modes, whose group velocity is within the solid angle selected by the detector aperture. Following procedure presented in [51], one can introduce the radiated power per solid angle in a coordinate space $dP/d\Omega$. This power gives a rate at which the dipole energy is transferred to modes with a group velocity pointing to the observation direction. The fact that due to the beam steering phenomenon several eigenmodes with different wave vectors, $\mathbf{k}_n^\nu$, can have parallel group velocity vectors, is taken into account by extra summation, ν, over all wave vectors for which $\hat{\mathbf{x}}\mathbf{V}_{n\mathbf{k}}^\nu > 0$ holds. $\hat{\mathbf{x}}$ is a unit vector of the observation direction.

Dipole moments of NC are randomly distributed in space. Consequently, the radiative power should be averaged over the all dipole moment orientations, hence, an ensemble of NC is equivalent to the set of point sources producing an isotropic distribution of wave vectors. An angular distribution of radiative power inside a PhC depends on the topology of the iso-frequency surface of the crystal at the emission frequency. A schematic view of the iso-frequency surface of an opal PhC is presented in Fig.13b for a frequency inside the Bragg gap. To plot the iso-frequency surface, one should calculate a PBG structure for all wave vectors within the irreducible Brillouin zone and then solve the equation $\omega_{n\mathbf{k}} = \omega_0$ for a given frequency ω_0. The iso-frequency surface at the Bragg PBG frequency of the opal deviates from a sphere mostly along the [111] axes, where the Bragg gap openings are located. In the vicinity to openings the iso-frequency surface forms a neck with the alternating negative and positive Gaussian curvature separated by parabolic lines with vanishing curvature. A small Gaussian curvature formally implies bunching of many Bloch

eigenwaves with different wave vectors travelling in the same direction due to the crystal anisotropy. Such concentration of radiated power along certain directions is a linear phenomenon and called the photon focusing [52].

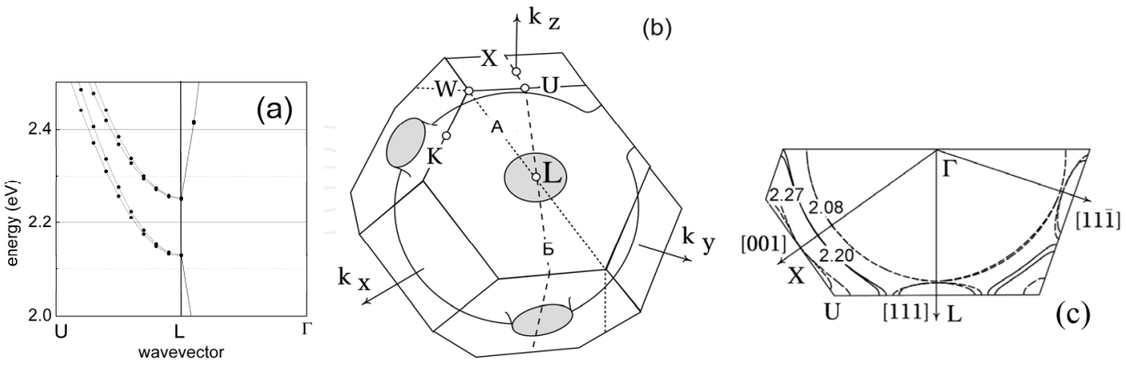

Fig. 13. Fragment of the PBG diagram along ΓLU cross-section. Frequency scale is adjusted to the discussed sample. (b) Illustration of the 3-dimensional iso-frequency surface of the 1st optical mode of an opal PhC for a frequency 2.2 eV inside the Bragg PBG inserted in the 1st BZ of the fcc lattice. (c) Cross-section of the BZ with iso-frequency contours at frequencies 2.08, 2.2 and 2.27 eV (compare to the diagram in panel (a)).

In Fig.13c the iso-frequency contours are presented for three different frequencies. They cut the Brillouin zone through the symmetry points X, U, L and Γ. One can assume that the experimentally measured far-field PL intensity represents the signal, which is averaged over different Brillouin zone cross-sections due to lattice disorder.

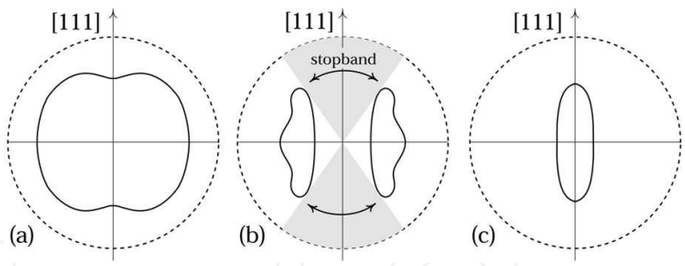

Fig. 14. Wave contours corresponded to frequencies 2.08, 2.2 and 2.27 eV (a, b, c respectively). Only the wave contours corresponded to the first and third bands are shown in the diagrams (a, b and c), respectively. Light grey region in (b) is the Bragg cone projection. A dashed circle is a wave contour in vacuum. Group velocity is plotted in the units of the speed of light in vacuum.

As the frequency remains below the gap, an iso-frequency contour is continuous and almost circular. The Gaussian curvature does not vanish for any wave vector. This implies a small anisotropy in the energy flux inside the crystal. It order to obtain the wave contour in coordinate space, one should plot a ray in the observation direction $\hat{\mathbf{x}}$ starting from the point source position and having the length of the group velocity $\left|\mathbf{V}_{n\mathbf{k}}^{\nu}\right|$. The calculation of the group velocity was discussed earlier in relation to schematics in Fig.10. The wave contour at 2.08 eV is single valued function of observation direction (Fig.14a). Fig.15 shows

the angular distribution of the radiated power for the same frequency. The latter is nearly isotropic and resembles, reasonably, the Lambert law (dashed line). To calculate the radiated power, one should sum over all optical modes, which are available at the given frequency.

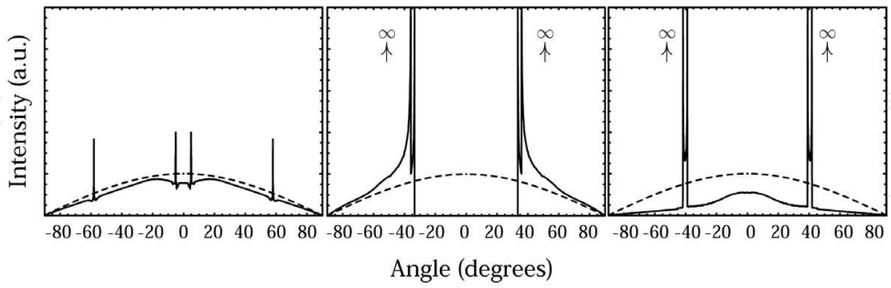

Fig. 15. Angular distribution of the radiated power for the same frequencies as in Fig.14. The radiated power in free space (Lambert law) is shown by dashed line for comparison.

With the frequency increase up to the midpoint of the first PBG, the topology of the iso-frequency contour abruptly changes. The gap developed along the ΓL direction and the iso-frequency contour becomes open (Fig.13c). This topological discontinuity results in a complex contour with alternating regions of different Gaussian curvature. Vanishing curvature leads to the folds of the wave contour (Fig. 14b). The folds in the wave contours yield that two Bloch modes are travelling in any observation direction outside the gap. Contributions from both modes should be taken into account, if the total radiated power is calculated. In the middle panel of Fig.15 the strongly anisotropic angular distribution of the radiative power corresponded to the 2.2 eV is presented, featuring zero intensity in the direction of the gap, and infinitely high intensity spikes in directions of folds of the wave contours occurring at, approximately, $\theta \approx \pm 40^o$ with respect to the [111] axis.

When the frequency crosses the upper boundary of the ΓL Bragg gap, i.e. the gap along ΓL direction closes, the 3rd and the 4th photonic modes come in consideration. In the Fig. 14c a wave contour of the 3rd band at 2.27 eV is depicted. It is single valued function elongated to the [111] axis, which leads to the preferable energy flux in this direction. An angular distribution of the radiative power at this frequency shows infinite intensity spikes at $\theta \approx \pm 40^o$ and a Gaussian-like lobe centred at $\theta = 0^o$ (Fig.15, right). An infinite intensity corresponds to the points of vanishing Gaussian curvature of the 1st and the 2nd photonic bands, while the central lobe is associated with the 3rd and the 4th bands.

Fig.16a shows experimentally obtained directionality diagrams in the vicinity to the Bragg gap. In the first approximation, these patterns satisfy the iso-frequency profiles (Fig. 13c) being the superposition of the isotropically distributed emission from a point source and the Bragg cones of the fcc lattice (Fig.13b). The next iteration takes into account the light focusing occurring due to uneven curvature of iso-frequency contours in a sense of diagrams in Fig.15. In fact, the emission from a thin film opal consists of isotropic unmodified (scattered and near-surface emission) and PBG-moulded ballistic components. The isotropic light source provides the background, the intensity of which varies as $\cos\theta$, and the ballistic component carries the fingerprint of the Bragg gap. Summing the diagrams of ballistic and diffuse components, the details of the experimentally obtained emission indicatrix can be accurately explained [53] (Fig.16b).

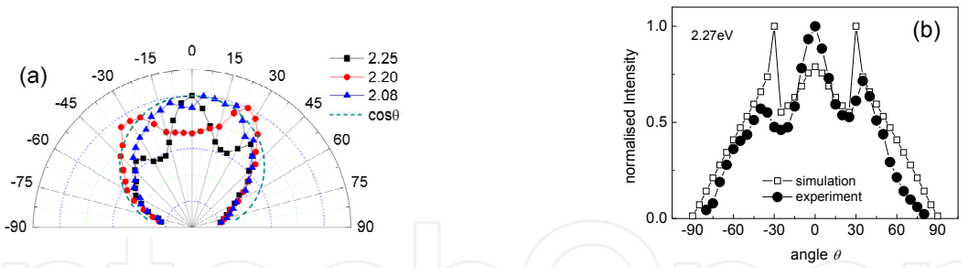

Fig. 16. (a) Directionality diagrams of the emission at specified frequencies across the PBG spectral range. Dashed line shows Lambertian distribution of emitted power. (b) Comparison of calculated and experimental emission directionality diagrams at $\hbar\omega = 2.27$ eV . Simulation includes emission focusing along special directions in the vector diagram. To match the experimental pattern a PBG-unaffected emission component has been added to the simulated pattern as the $\cos\theta$ background.

7. Emission of nanocrystals in inverted opals

Reduction of the volume fraction of "heavy" dielectric compared to that in opals assembled from spheres favours the wider PBG opening [54]. The inverted opals prepared by impregnation of the opal voids with another dielectric and subsequent removing the opal spheres offer such enhancement of PhC performance. Therefore, it is reasonable to examine the luminescent properties of the NC CdTe in the inverted opal. Usually, the semiconductors are used for opal inversion. The close vicinity of NCs to the surface of semiconductor brings another complication to the radiative energy relaxation due to energy transfer between the NCs and the semiconductor. In this section we will consider both aspects of NC to PhC interaction.

TiO_2 inverted opals were prepared by templating in thin film opals. As a first step, opal films consisting of approximately 15-20 monolayers of 300 nm diameter monodisperse polymethyl methacrylate (PMMA) beads were prepared by slow-drying of a sphere suspension on microscope slides. Then these films were dipped into a solution of $TiCl_4$ in HCl, followed by a moisture-promoted hydrolysis and heating at 160°C for 1 h. At this stage, an interconnected TiO_2 framework is formed in the voids between the PMMA beads. After dissolving the polymer beads in tetrahydrofurane, TiO_2 inverted opal films were formed (Fig.17a). The reflectance spectra of the TiO_2 inverted opal display a pronounced (111) diffraction resonance indicating a directional PBG. Its angular dispersion follows the Bragg law (Fig.17b). The strong deviation from a diffraction on (111) planes occurs around $\theta = 40^o$ due to the multiple wave diffraction at anticrossing of (111) and (200) resonance dispersions [55]. The relative full width at half maximum (FWHM) of the reflectance peaks is about 10 % (15% in transmission) compared to 5.6 % in opals [56]. Owing to a broader gap, the spectral overlap of pseudogaps along different directions of the Bragg resonance in TiO_2 opal is remarkably larger than in PMMA template. Simultaneously, the Bragg cones are also larger. These factors are particularly important since increasing both, spectral and spatial PBG dimensions is a pre-condition of stronger modification of emission of PhC-embedded light sources.

To realize a PhC light source, a small amount of colloidal CdTe NCs stabilized by thin organic shells was embedded into the replica pores by soaking the films in dilute aqueous colloidal dispersions. CdTe NCs of 3 nm in diameter were used to fit the emission band to the Bragg

PBG of TiO_2 inverted opal. After drying, the CdTe NCs remained attached to the inner surface of the TiO_2 frame through electrostatic interaction with functional groups of thiol stabilizers.

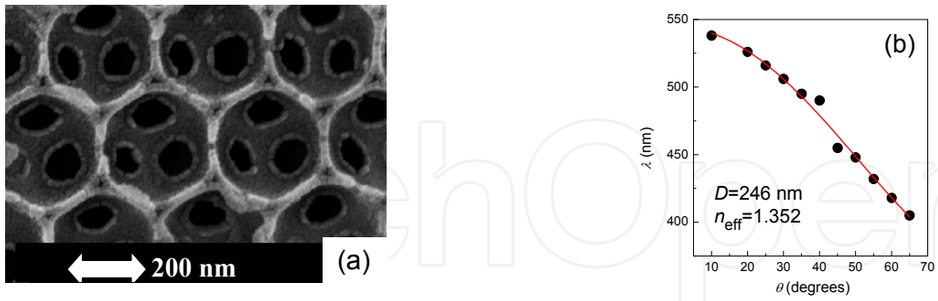

Fig. 17. (a) SEM image of inverted TiO_2-opal. (b) Angle dispersion of the (111) resonance in TiO_2-opal (points) and its approximation by the Bragg law. The diameters of spheres and the effective index of refraction extracted from the Bragg fit are shown.

PL spectra were measured at T = 300 and 18 K under cw excitation by the 457.9 and 351.1 nm lines of an Ar^+ laser. The excitation power was varied between 10^{-5} and 10^{-1} W. PL spectra were recorded in the front window configuration thus allowing the emission to traverse the film. The emission was collected within a 4° solid angle along the direction defined by angle of θ with respect to the [111] axis of the opal fcc lattice.
Under 457.9 nm excitation the PL spectrum at T = 300 K exhibits a band with a maximum at 2.38 eV and a FWHM of 0.26 eV. Under 351.1 nm excitation this band becomes broader and shifts up to 2.44 eV. At T = 18 K this PL band shifts further to 2.47 eV, but its bandwidth is ~1.5 times narrower (Fig.18a). In fact, the low temperature PL band (curve 3) resembles that observed in the NC suspension, where NCs are relatively isolated from the environment. Such evolution of NC emission with changing the excitation conditions has been ascribed to the NC-substrate interaction [57,58]. It is suggested that the TiO_2 template provides a potential relief due to surface defects, which co-ordinates the deposition of NCs.

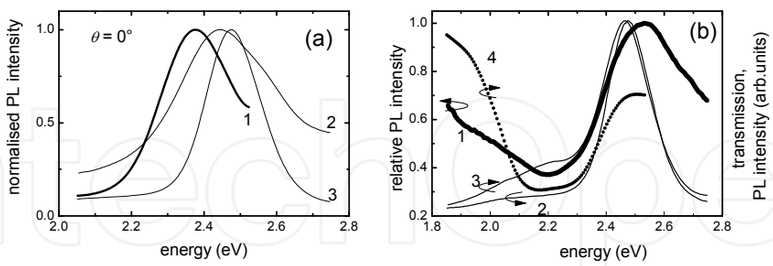

Fig. 18. (a) PL spectra of the CdTe NC-TiO_2 inverted opal at θ = 0° under 457.9 nm and 351.1 nm line excitation at T = 300 K (curves 1, 2, respectively) and at T = 18 K (3). (b) Relative PL spectrum (curve 1) of the CdTe NCs-TiO_2 opal obtained as the ratio of PL spectra at θ = 0° (2) and 70° (3) compared to transmission spectrum (4).

The TiO_2 framework itself has its electronic bandgap at about 3.1 eV thus facilitating the absorption of the 351 nm radiation and enhancing the energy exchange with CdTe NCs. It is further helped by the fact that the band edge emission from TiO_2 is above the spectral range of CdTe PL band. On the other hand, the polymer shells of NCs reduce the energy exchange. Nevertheless, defect states at TiO_2-CdTe interface trap the photogenerated electron-hole

pairs in polymer-capped NCs by, e.g., dissociation of excitons [59]. In turn, the radiative recombination of trapped carriers leads to broadening of the observed PL band by an amount comparable to the trap energy range. The narrowing of the NC PL band at low temperature can be understood as the result of reducing the contribution of trapped excitons to the emission flux due to increasing their lifetime. This observation emphasises that the emission of CdTe NCs in TiO_2-opal involves multiple-level relaxation of electronic excitations i.e., this system cannot be treated as a two-level system.

The relative PL spectrum for θ=0° contains the minimum, the position of which is in good agreement with the (111) Bragg gap in the transmission spectrum. As the reference, the PL spectrum of the same sample obtained at θ = 70° was used (Fig. 18b). The slight dissimilarity of pseudogaps in the transmission and relative PL spectra is due to (i) the difference in coupling of externally (outside the PhC) and internally (inside it) generated light to eigenmodes of the PhC and (ii) the unaffected near-surface emission coupled to free space modes.

The input-output characteristics of CdTe-TiO_2-opal [60] are similar to that of the CdTe-opal (section 5). The P_0 spectrum shows a maximum at the bandgap frequencies (Fig.18). This maximum appears more pronounced under UV-excitation because it is no longer overshadowed by the overlapping minimum, which is blue-shifted following the shift of the PL maximum. A comparison of P_0-spectra obtained at different angles of detection demonstrates that the maximum follows the PBG dispersion and vanishes gradually at larger angles θ of detection, whereas the minimum remains unchanged. The difference with the CdTe-opal sample (section 5) is almost 2-fold increase of the PBG width.

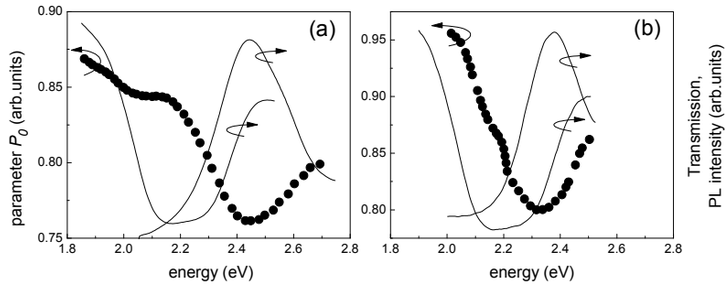

Fig. 19. (a, b) Parameter $P_0(\hbar\omega)$ (dots) in comparison to transmission and PL spectra obtained at $\theta = 0^o$ for excitation by (a) 351.1 and (b) 457,9 nm lines.

The interplay of the minima and maxima in P_0 spectra shows that (i) the minimum corresponds to the faster saturation of spontaneous emission in the PL band maximum that is determined by higher matrix element for electron transitions between excited and ground states in the electronic band structure of the NC, whereas (ii) the maximum results from the emission stimulation due to stronger NC to optical mode coupling provided either by slow propagating modes or localized defect modes.

The drawback of studied inverted opal is higher amount of defects compared to the opal template. These extra defects are added due to inhomogeneous infiltration of the opal voids and uncontrollable lattice contraction due course of annealing. Moreover, the higher refractive index contrast in the TiO_2 opal replica compared to the opal template leads to stronger distortion of the EM field distribution around the defect. This leads to emission losses, e.g., the emission initially radiated to PhC eigenmodes experiences higher chance to be scattered in the Bragg cone [61] and

to be transported by defect modes. Since the stimulation takes place only for modes in the PBG direction, this effect becomes buried in the diffuse radiation, leading to suppressing the P_0 peak in the PBG interval. Hence, in spite of higher strength of the PBG effect in studied inverted opals, the emission enhancement becomes counteracted by the influence of disorder.

8. Emission of nanocrystals in hetero-opals

The main idea behind PhC heterostructures is to bring two different PhC in contact (Fig.20a) [62]. The obvious consequence of heterostructuring is the fingerprints of two [63] or more PBG structures in the optical properties. Such a structure contains the interface, which implies a sharp step in the spatial distribution of the EM field. In spite of the fact that the geometrical "thickness" of the interface is less than the light wavelength, the transition region is formed in the vicinity of the interface due to the EM field continuity and a need of light coupling from modes of one PhC to modes of the other. In this region, which extends over several lattice periods, one can expect special conditions for the light propagation [64]. Hetero-opals can be used for achieving a control upon the emission characteristics [65] if one of the opals is infilled with light-emitting NC and used to control the NC-to-mode coupling (opal-source) and another is used to shape the emission spectrum according to its PBG (opal-filter). It appears that the properties of such hetero-opal differ from the linear superposition of properties of the source and filter opals due to the interface interaction [66]. However, the light coupling at the interface remains so far largely unexplored issue [67].

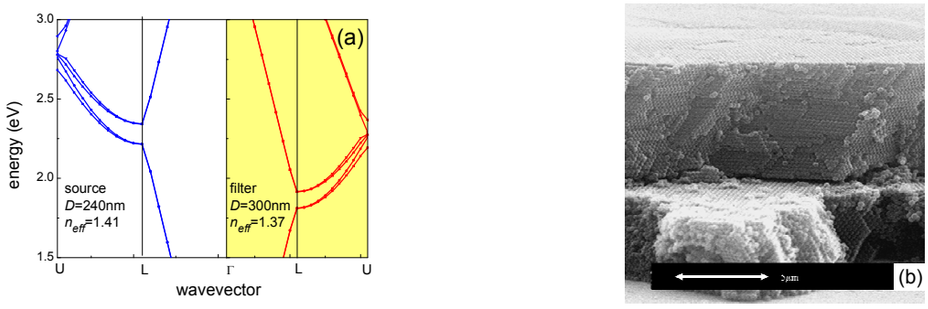

Fig. 20. (a) Band diagrams of the opal-source and the opal-filter in contact. (b) SEM image of the hetero-opal assembled successively from two opal films crystallised from latex spheres of 240 and 300 nm in diameter.

The examined hetero-opal was prepared using the successive assembling of opal films [68]. Opal films studied in this work were grown on glass or quartz slides by crystallization of polystyrene (PS) beads ranging from 240 to 450 nm in diameter. Aqueous 1-5 vol.% colloidal suspensions of PS beads were placed in a Teflon cylindrical cell (7 mm inner diameter) and then the solvent was evaporated under moderate flow of warm air. Typical thickness of opal films was 5-10 μm. The sintering at 90° for 1 h was applied to allow further treatment of films.
Sandwich-type hetero-opals were prepared by self-assembling the top opal film on the surface of the bottom opal film, which was crystallized previously from beads of another diameter. Fig. 20b shows SEM image of a hetero-opal with the bottom film consisting of D=240 nm and the top film – D=300 nm beads. Here and below, we denote this structure as

the 240/300 nm opal. The abrupt interface between films indicates that the formation of the top film proceeds independently on the geometrical profile provided by the bottom one.
The layer-by-layer (LbL) deposition technique, which is based on alternating adsorption of layers of oppositely charged species on the surface, was used for impregnation of opal films with CdTe NCs. LbL technique was originally developed for positively and negatively charged polyelectrolyte pairs [69] and then extended to the assembly of polymer-linked NCs [70]. This method was successfully applied to a variety of substrate materials with flat and highly curved surfaces [71]. Following LbL procedure, the substrate with an opal film was immersed for 30 minutes in a 5 mg/ml aqueous solution of poly(diallyldimethylammonium) chloride (positively charge polyelectrolyte), then thoroughly washed and immersed for 30 minutes in a 10^{-3} M aqueous solution of CdTe NCs capped with thioglycolic acid and, thus, carried a negative charge at appropriate pH [72]. 0.2 M of NaCl was added to both solutions to facilitate a formation of smooth layers. Moderate stirring was applied to solutions to accelerate the mass transfer. Because opal voids are either of 0.41 or 0.23D in size and connected via 0.15D channels [11], both polyelectrolyte molecules and CdTe NCs can easily access internal pores. We assume that the in-void coating proceeds in the same manner as a deposition on the open surface. The LbL procedure was repeated several times to increase the amount of deposited CdTe NCs. The NC-polyelectrolyte layer formed on the opposite side of the slide was finally removed by washing in acetone and ethanol.
The LbL deposition provides uniformity of the coating thickness and NC environment (Fig.21a), as compared to a direct infiltration of NCs into opals. No leakage of NCs from the bottom opal film back to water takes place during the deposition of the second film judging from the absence of the luminescence of the background solution. Anchoring of NCs is also required to prevent their diffusion to another film of a hetero-opal. The important condition is the need for the emission spectrum of NC to overlap both PBGs in the hetero-opal. Correspondingly, CdTe NC of 2 and 5 nm with respective emission bands centred at 2.29 and 2.08 eV were explored.

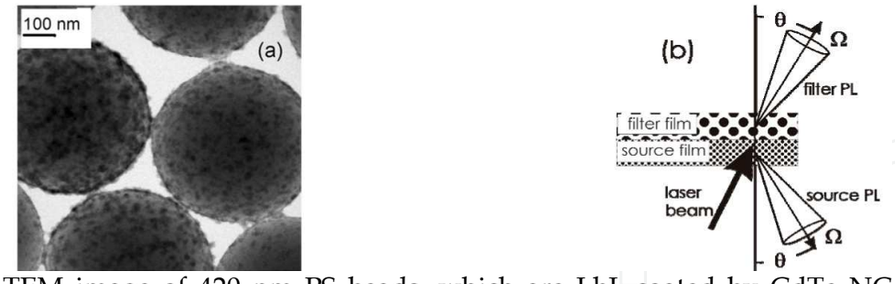

Fig. 21. (a) TEM image of 420 nm PS beads, which are LbL-coated by CdTe NCs in one deposition circle. The NCs appear darker due to the higher contrast. (b) Layout of the PL measurements. θ - the angle of incidence and the angle of detection, Ω - the solid angle of the light collection.

A straightforward consequence of the PBG anisotropy in hetero-opals is the spectral and spatial anisotropy of the PL of NCs embedded therein. In Fig. 22 the source and the filter PL spectra are shown in comparison to transmission spectra at different angles of the light detection to demonstrate the correlation between the emission minimum and the corresponding Bragg gap. It is instructive to emphasize the different physical origin of this

minimum in the source and the filter PL spectra. The directional minimum of the source PL spectrum is a consequence of the lower mode number available for coupling with emitter within the PBG bandwidth along a given direction. In contrast, the minimum in the filter PL spectrum appears due to the back-reflection of the source radiation from a filter film within the PBG bandwidth of the filter, which does not directly affect the LDOS in the source. In other words, the origin of the filter PL minimum is the same as that of the transmission minimum. The diffuse scattering of emitted photons at the interface and in the filter film can be the reason for the absence of the source PBG minimum in the filter PL spectrum.

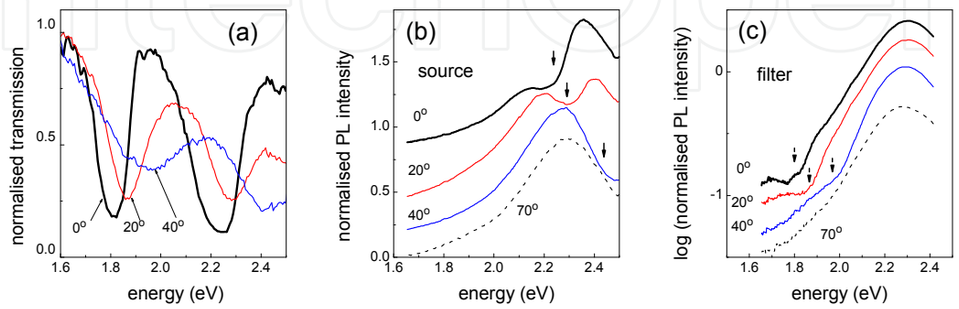

Fig. 22. (a) Spectra of transmission of the 20 μm-thick 240/300 nm source-filter hetero-opal obtained along different directions that are labelled by the angle. (b,c) Source and filter PL spectra of a hetero-opal with 2 nm NC in the source film, respectively. Curves in the panels are shifted vertically for clarity. Dotted line shows The PL spectrum obtained at 70° that is used as a PBG-unaffected reference.

Transmission minima for the light propagating normally to the film planes are centred at 1.81 and 2.24 eV and the FWHM of these resonances is about 9% in transmission (Fig.22a). The transmission minima in such hetero-opals can be traced down to 60° due to the limit applied by enhanced scattering at the interface. The PL spectra of the source and filter films demonstrate minima in agreement with transmission spectra (Fig.22a). The relative PL spectra from the source and filter sides of the hetero-opal demonstrate two minima for the larger NC. These minima can also be noticed in the PL spectra of smaller NC (Fig.23).

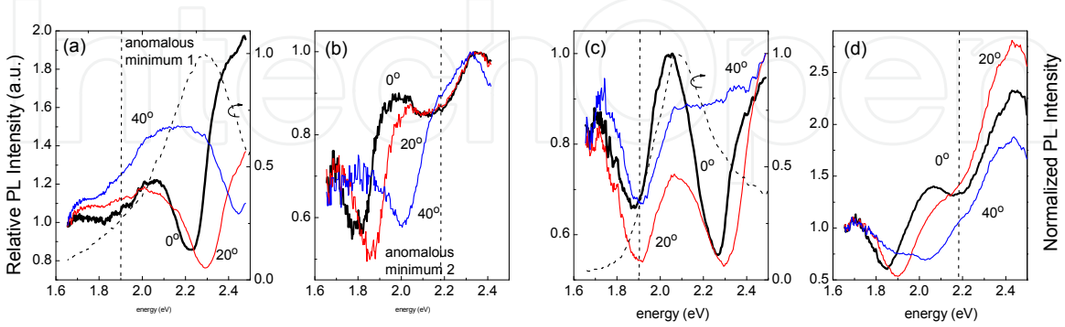

Fig. 23. Relative PL spectra of the source (a, c) and filter (b, d) at different detection angles for NC of 2 (a,b) and 5 nm (c,d) with PL bands centred at 2.29 and 2.08 eV, respectively. Angles are indicated at curves. Dashed PL spectra are obtained at 70°. All spectra are normalised to achieve the same intensity at the "red" edge. Vertical dashed lines indicate the position of "anomalous" minima.

One minimum in relative source and filter spectra moves towards higher energies with increase of the detection angle in accord with the "blue" shift of the (111) Bragg gap. The relative midgap suppression of PL intensity at θ=0° is about 50%. However, the second minimum marked by a dashed line is a stationary one, which shows no shift with changing the angle of detection (Fig. 23). Interestingly to note, that the emission attenuation in the directional and stationary minima are comparable in the case of the 5 nm NCs, the PL intensity of which is evenly distributed between filter and source PBG minima.

Experimental findings so far can be summarized as followed. (a) The emission from the hetero-opal acquires the artificial anisotropy due to the difference of directional Bragg gaps. Important, that this anisotropy is fully under control because the PBG frequencies in a bi-layer opal directly relate to the sphere diameters. (b) The emission spectra acquire the additional non-dispersive minimum, the position of which is correlated but does not coincide with the directional minimum of another opal in a heterostructure. Since such effect was not observed in single light emitting films, its appearance is reasonable to assigned to the light coupling at the interface. The fact that the position of non-dispersive minima is not sensitive to the change of the NC emission band supports this assumption. If so, the spectrum transformation after internally generated light crossing the interface looks like loosing the memory about the PBG directionality.

In order to illustrate this conclusion the angle diagrams of the emission intensity obtained from the source and filter sides of the hetero-opal are compared in Fig.24. The diagrams of the source change their shape like it was discussed with respect to the single light emitting opal film (section 6, Fig.16), moreover, they are broader than the Lambertian diagram. Oppositely, the diagrams of the filter are almost insensitive to changing the frequency and appear much narrower compared to the Lambertian shape. Such phenomenon can be considered as the emission focusing. Such focusing should be controlled by the difference in opal film lattice parameters.

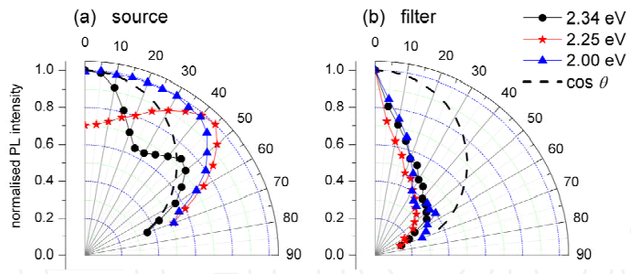

Fig. 24. Emission indicatrices of the normalised to the maximum emission intensity at different frequencies from (a) the opal source and (b) the opal filter in the vicinity to (111) resonances in the 240/300 nm hetero-opal. Dashed line shows the Lambertian diagram.

One can raise a question concerning the mechanism of the emission flux formatting. On the one hand, the absence of memory about the source PBG points to the diffuse character of photon propagation. However, the scattering in the volume of the source (thickness ~14 μm) is not sufficient for complete randomising of the emission flow as demonstrated by the source diagrams. In contrast, the light crossing of the hetero-interface is considered as the sequence of scattering of the incident light, which is transported by the Bloch modes of the source PhC, and following coupling of scattered light to the Bloch modes of the filter PhC [64]. The interface scattering occurs due to the symmetry mismatch between two reservoirs

of modes in these PhC lattices. Hence, a fraction of the source radiation propagates to the detector as coupled to the filter eigenmodes and the other fraction – as the uncoupled decaying modes. Therefore, the formatting of outgoing flux proceeds accordingly to the interface coupling conditions, moreover, it is associated with light losses. On the other hand, the light coupling is controlled by the iso-frequencies of two PhC in contact. Fig.25 illustrates this process. In particular, the light propagation from the source with a spherical iso-frequency surface is allowed to all but the directions in the Bragg cones of the filter. With the increase of the emission frequency above the PBG in filter and source crystals, the corresponding iso-frequency surfaces acquire the complex profile leading to rapid variation of the coupling conditions with the frequency.

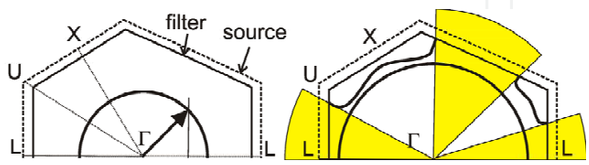

Fig. 25. Schematics of the iso-frequency surfaces in two PhCs with slightly different lattice parameters and the same effective refractive index. (a) Omnidirectional coupling at frequencies below the 1st bandgap in both PhCs. (b) Directional coupling of the emission generated in a source crystal at the frequency below its 1st bandgap to the filter film at the frequency within its 1st bandgap. Shaded cones are the Bragg cones.

The intensity of scattered radiation increases in the source PBG interval with the increase of the angle of light incidence at the interface [73], hence, progressively lower flux couples to the filter. Since scattering equalises the angle distribution of the PL intensity over all directions bringing its spectrum in agreement to the direction-independent DOS spectrum, this is observed in the relative PL spectra of the filter as the anomalous non-dispersive minimum. Thus, effectively, the moving filter PBG minimum squeezes the emission diagram towards the stationary source-related minimum leading to the efficient compressing the filter diagram.

It is instructive to represent the emission anisotropy as the filter-to-source intensity ratio (the anisotropy factor). Such ratio shows a minimum in the filter (111) PBG and the maximum in the source (111) PBG, the spectral separation of which depends on the lattice parameters of the hetero-opal crystals (Fig.26). While this ratio quantifies the emission anisotropy, it is not possible to pin down its absolute value because the substrate introduces the asymmetry in emission outcoupling in a hetero-opal.

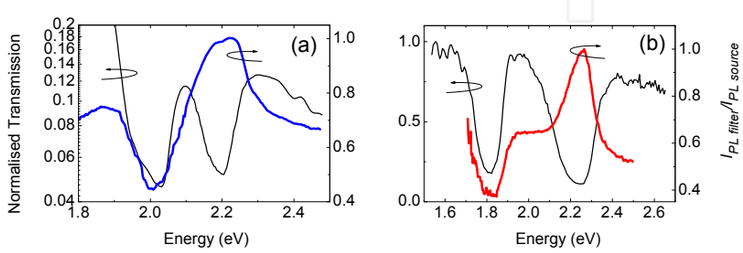

Fig. 26. Anisotropy factor for the source-filter hetero-opals assembled from (a) 240/269 and (b) 240/300 nm opals along the [111] direction.

The shape of the anisotropy factor spectra changes dramatically with the increase of the excitation power and the detection angle. Along the film normal, the minimum of anisotropy factor for the filter remains unchanged along the pumping increase, whereas the maximum for the source PBG monotonously decreases (Fig.27a). The reason of this effect is the stimulated emission in the source (compare to Fig.12c) and the absence of amplification in the filter opal. Along the detection angle increase this picture changes. At $\theta = 20^o$ (i) the extrema of the anisotropy parameter shift to higher frequencies according to PBG dispersions, (ii) the filter minimum becomes also pumping-dependent and (iii) the transition region between resonances becomes distorted. At $\theta = 40^o$ (i) the maximum of anisotropy parameter in the source PBG is replaced with the maximum in between filter and source PBGs and (ii) with the increased pumping the emission anisotropy reduces by three times in its maximum. At $\theta = 70^o$ the pumping dependence of anisotropy disappears and the anisotropy spectrum becomes $\propto 1/I_{PL}(\hbar\omega)$ (Fig.27d).

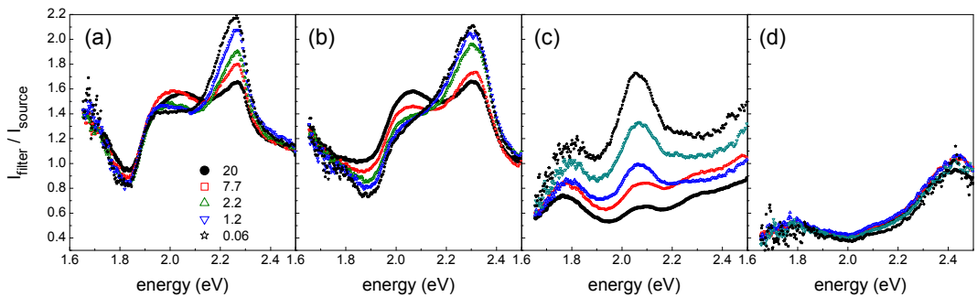

Fig. 27. Evolution of the anisotropy parameter with the increase of the excitation power for different detection angles. The excitation power is specified in the legend in panel (a). Panels (a-d) correspond to the detection angles 0, 20, 40 and 70o.

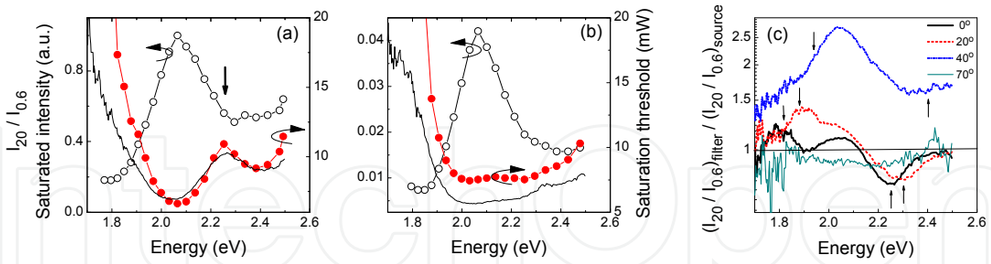

Fig. 28. Spectra of the saturation threshold (circles) and the saturated emission intensity (open circles) for the (a) source and (b) filter opals at $\theta = 0^o$. The ratio of the PL spectra obtained at pumping powers 20 and 0.6 mW are shown by lines for comparison. The arrow in (a) indicates the (111) source PBG. (c) Spectra of enhancement anisotropy parameter for different detection angles. Up- and down-arrows shows PBG of the source and the filter, respectively.

Spectra of the emission anisotropy parameter obtained at 40o show that the emission intensity passed through the interface in the spectral interval between filter and source PBGs (centred at ~2.1 eV) becomes relatively lower with at the increase of the pumping power. This observation reveals an important consequence of the interface coupling – the intensity

of the source PL in this range increases much faster compared to that passed through the filter. This non-linear effect can be associated with the increase of the light path in the gain medium of the pumped source opal film. We mentioned that the transmittivity of the interface is much lower for the oblique incident light because of increased interface scattering with possible trapping of scattered light with PBG frequencies at the interface [73]. Taking into account the emission spectrum having the maximum at ~2.05 eV, it is possible to conclude that the scattered radiation is responsible for the source PL increase and that this increase is correlated with the gain spectrum (Fig.23c).

The estimate of the emission rate changes made by using the emission saturation threshold agrees the above picture. The peak in $P_0(\hbar\omega)$ of the source opal coincide the source PBG, whereas no clear features is observed in the spectrum of this parameter for the filter emission (Fig.28a,b). Similarly the spectrum of the ratio of PL intensities measured under pumping of different powers reasonable well corresponds to the $P_0(\hbar\omega)$ spectrum (section 5.2). Then the expression $\left(I_{20}/I_{0.6}\right)_{filter}\Big/\left(I_{20}/I_{0.6}\right)_{source}$ allows to quantify the spectrum of the anisotropy of the emission stimulation (Fig.28c). Since the parameter of enhancement anisotropy is almost 1 for the $\theta = 70^o$, where no PBG influence is expected, it produces the absolute value of enhancement. At $\theta = 0^o$ and 20^o one can see the 1.5 time enhancement in the source PBG and the emission suppression in the filter PBG. This once again points to the influencing of the NC emission by filter PBG. At higher angles the influence of PBG becomes indistinguishable compared to the 2.5 times enhancement of the interface-trapped emission at 2.05 eV. It is worth noting that the development of the latter band is detectable at lower angles as well, but its magnitude is comparable to the PBG enhancement. Looking back to Fig. 27, this enhancement is the reason for the corresponding peak of the anisotropy parameter.

9. Modification of nanocrystal emission by the local field of colloidal crystals

The control over the emission spectrum and directionality of light sources can be achieved by tailoring their EM environment, as discussed earlier [3,4,7,6]. So far we considered the emission of sources embedded in opals. Such configuration leads, in the first instance, to the PBG-related suppression of spontaneous emission due to reduction of the mode density and pushing emission flow away from the PBG direction. Simultaneously, the emission coupled to the resonance modes in the same PBG interval experiences stimulation. At the PhC surface the strong local fields are developed at PBG frequencies. The local field pattern of colloidal crystals has been visualized using the near-field optical microscopy [74,75]. Although such field exponentially decays with increasing the distance from the PhC surface, it can promote the emission from NC within the wavelength-scale distance [76]. If so, the fraction of the enhanced emission will be added on top to the spontaneous emission of NC in contrast to the case of the PhC-embedded NCs, when the stimulated emission is added on top of the suppressed spontaneous emission (Fig.29a).

The idea of the spatially separated NC-PhC light source is shown in Fig.29b. In such configuration the dipole transition probability of an oscillator placed in between a 2D PhC and a dielectric substrate depends on the NC location with respect to nodes and antinodes of the EM field, hence, the emission of a light source radiated in the near-field zone of the PhC can be either enhanced or suppressed, but the enhancement effect prevails [77,78].

The PBG emission enhancement should not be confused with traditional ways of increasing the brightness of light emitting devices based on grating couplers and randomly textured surfaces [79,80]. These techniques increase the external quantum efficiency by extracting that fraction of emission, which is normally trapped in the structure due to the total internal reflectance. With the increase of the refractive index contrast, such gratings can be considered in terms of a slab 2D PhCs, in which the wave optics phenomena co-exist with geometrical optics [81]. To date, the efficient out-coupling of radiation has been realized by coupling the radiation to leaky guided modes with frequencies above the light cone in emitters nanopatterned as 2D PhCs [82].

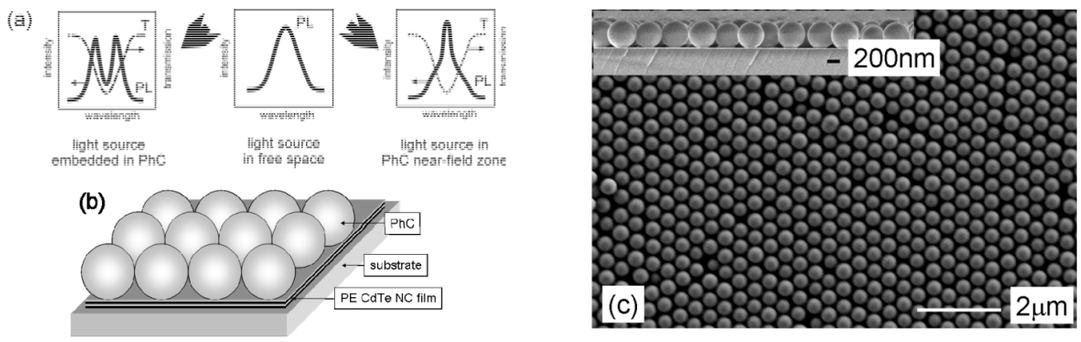

Fig. 29. Schematics of the emission spectrum modification for the light source inside a 3D PhC (left) and at the PhC slab surface (right). Note the different origins of the transmission minima. On the left it occurs due to diffraction at the stack of crystal planes. On the right it occurs due to excitation of leaky guided modes at the PhC surface. (b) Schematics of the structure consisted of a glass substrate with LbL-deposited CdTe NC and LB deposited monolayer of silica spheres. (c) SEM image of a LB monolayer of 519 nm silica spheres on a glass substrate. Inset: the SEM side view of LB monolayer.

From a technology point of view sandwiched NC-opal structures look simpler compared to NC-impregnated opals. However, the light source should be thin enough to be accommodated in the near-field zone of the PhC (Fig.20c) [83].

9.1. Transmission, diffraction and photoluminescence spectra of sandwich sources

Uniform thin films containing 2 nm CdTe NCs [84] were prepared by LbL assembly [85]. The following cyclic procedure was used: (i) dipping of the glass substrate into a solution (5 mg/ml in 0.2 M NaCl) of poly(diallyldimethylammonium chloride) (PDDA) for 10 min, (ii) rinsing with water for 1 min; (iii) dipping into aqueous suspensions of the negatively charged NCs (ca. 10^{-6} M) for 10 min; (iv) rinsing with water again for 1 min. Each cycle of this procedure results in a 'bilayer' consisting of a polymer/NC composite. 20 bi-layers were deposited in order to increase the brightness of luminescence. The thickness of a 20 bi-layer film is about 60 nm. Since the volume fraction of NCs is about 27%, the average RI of the PE-CdTe film is about 1.9. In what follows these films are referred as NC films (NCFs).

Silica spheres of the nominal diameter D=519 nm were hydrophobised with 3-trimethoxysilylpropyl methacrylate. The Langmuir-Blodgett (LB) technique, with a low barrier speed of 6 cm^2 min^{-1}, was used to compress sphere arrays in hexagonally packed monolayers (1L) on the surface of doubly distilled deionised water and to transfer them to

the substrate. Using this technique, the monolayer of spheres was deposited at a surface pressure of 4mN/m [86] on to the LbL NCF substrate (inset, Fig.2). Subsequent monolayers were deposited after drying the deposited ones. Both mono- and multiple-layers (up to five layers (5L)) of the SiO_2 spheres were prepared. Monolayers of spheres form the LB colloidal PhC possessing the PBG of (2+1)-dimensionality. Although no 3D lattice is formed due to the lack of lateral alignment between monolayers, the LB crystal remains ordered within each monolayer of spheres and as a periodic stack of monolayers [87,88].

The PL spectra of NCFs were excited by the 457.9 nm line of an Ar-ion laser. A laser spot size of 5 mm in diameter was selected in order to mimic the emission from a large-area display. The excitation conditions – the laser power and the spot size, were maintained constant at all angles of the detection in order to eliminate excitation-related variation of the PL spectra (Fig.4b). The light collection cone was restricted to 6° by an aperture between the sample and collecting lens. Emission was collected in the forward direction by exciting the NCF through the substrate and detecting after passing the PhC film and in the backward direction – similarly excited but not traversed the PhC film.

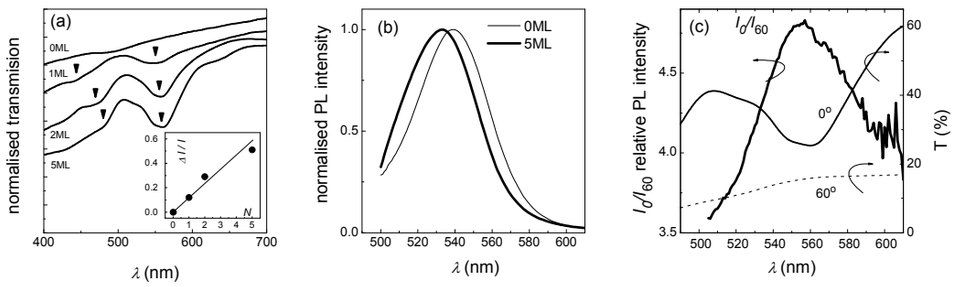

Fig. 30. (a) Transmission spectra of samples with different number, *N*, of sphere monolayers along the LB crystal normal. Inset – relative light attenuation at the transmission minimum as a function of *N*. The short wavelength minimum is the result of the resonance splitting in symmetric and antisymmetric combinations. This splitting decreases along the increase of the number of monolayers. (b) Normalized PL spectra of bare NCF (thin line) and 5L LB-coated NCF (thick line) at $\theta = 0^o$. (c) Relative PL spectrum in comparison to far-field transmission spectra obtained at angles $\theta = 0^o$ and 60^o.

The *s*-polarized far-field transmission spectrum of the 1ML sample at $\theta = 0^o$ on a glass substrate (Fig.30a) shows the well-defined minimum of 0.08 relative FWHM centred at 548 nm, which provides 12% attenuation of the incident light. The central wavelength of this minimum increases slightly with the increasing number of layers, N. For multiple layer coatings, the transmission significantly decreases towards shorter wavelengths due to light scattering at package irregularities. Transmission spectra of multilayers demonstrate the increase of the relative attenuation $\Delta I / I_0$ with increasing N as $\Delta I / I_0 \sim N^{0.9}$ (inset Fig.30a), where I_0 is the extrapolated transmission in the absence of the minimum. This, practically, linear dependence shows that the attenuation in the LB crystals is an additive function per number of layers. Additional shallow minima were detected at, approximately, 444, 470 and 481 nm for the 1L, 2L and 5L samples, respectively (Fig.30a). The 2L and 5L samples also possess the transmission minimum centred at 1093 nm due to the Bragg diffraction on a stack of monolayers [87], which is not shown.

Fig.31a,b shows the angular dispersion of the transmission minima in a 2L LB-NCF sample. There are I, II, III, IV branches of minima, which are degenerate at $\theta = 0^o$. Calculated dispersion of leaky guided modes in a 2D grating is superimposed on the transmission pattern. The correspondence is observed only between I and (1,0) in s-polarised light and between III and $(0,\bar{1})$ branches in p-polarised light.

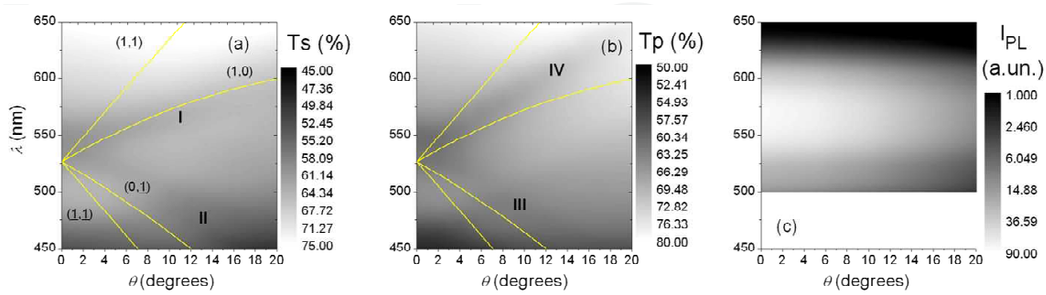

Fig. 31. (a, b) Transmission spectra of CdTe-1L-LB sample under s- and p-polarised light. Rome numbers denote the transmission minima. Lines are calculated eigenmodes of 2D slab PhC possessing the hexagonal lattice of scatterers and the effective refractive index of the 1ML of silica spheres. (c) The PL band of this sample.

The emission band of the NCF assembled from 2 nm NCs is centred at 540 nm (Fig.30b) and possesses the 0.085 relative FWHM. At $\theta = 0^o$ the emission band of the 0.09 relative FWHM of the 5L-LB NCF is centred at 533 nm. The blue shift of the emission band of the LB-NCF sample with respect to that of the bare NCF is the result of the LB coating as was proved by the multiplication of the PL spectrum of the bare NCF by the transmission spectrum of the 5L LB that reproduces such bandshift. The broadening of the PL band of LB-NCF sample could be induced by the chemical modification of the NC surface during the course of the LB film deposition. PL spectra of the LB-NCFs look similar for the different number of LB monolayers. The relative PL spectrum $I(\lambda)_{\theta=0} / I(\lambda)_{\theta=60}$ shows the maximum centred at 555 nm, which coincides with the minimum of the transmission spectrum (Fig.30c). The angle-resolved PL spectrum at $\theta = 60^o$ was used as the reference (Fig.30c).

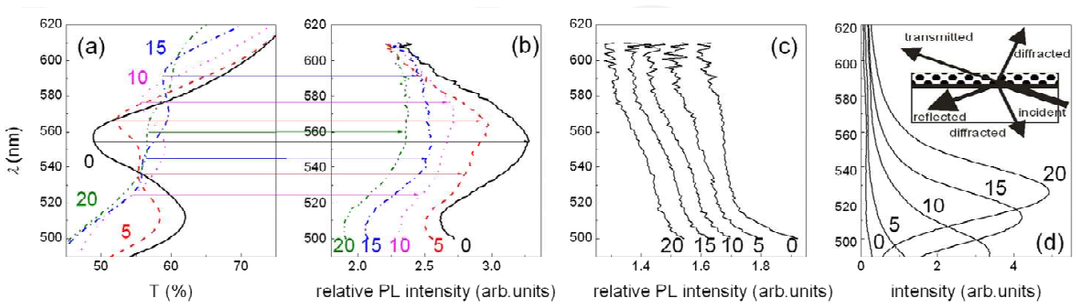

Fig. 32. (a) Angle-resolved transmission spectra of 2L LB-NCF under s-polarized light. Numbers show the angles of light incidence. (b) Angle-resolved relative PL spectra. Numbers show the detection angles. Arrows indicate the correspondence between transmission minima and PL bands. (c) Angle-resolved PL spectra of the uncoated NCF. Numbers show the detection angles. (d). Diffraction spectra at angles α shown at curves. Inset: Schematics of the light transmission and the first order diffraction in LB coating.

The overlap of the PBG with PL band takes place at $0^o \le \theta \le 20^o$ (Fig.31). It is immediately seen that the PBG effect upon the emission intensity is small. Over this range the maxima in the relative PL spectra correlate the minima of the transmission spectra (Fig.32 a, b). It is worth noting that the PBG-related modulation of the PL intensity is proportional to the attenuation in the transmission minimum (Fig.32a,b). In the case of the uncoated NCF no angular dependence of the PL spectrum was detected (Fig.32c)

9.2. Emission indicatrix

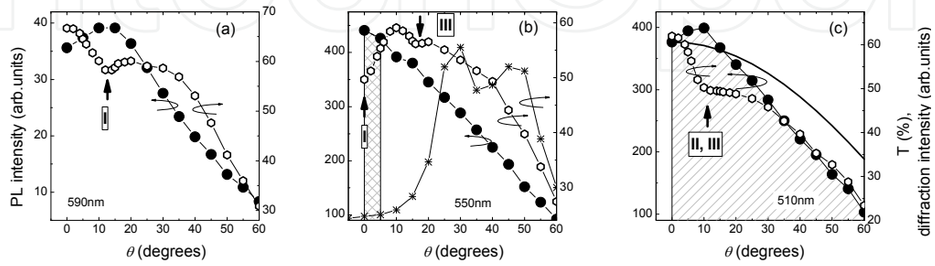

Fig. 33. Angle diagrams of emission intensity (solid circles) at $\lambda = 590, 550$ and 510 nm in comparison to transmission diagrams (open hexagons). These diagrams are compared to the angle diagram of diffraction intensity at $\lambda = 550$ nm (stars) in panel (b) and the Lambert diagram (line) in panel (c). Shaded areas show the emission power between 0 and 5o - S^5_{550} (b) and 0 and 60o - S^{60}_{510} (c). Arrows mark the angle position of transmission minima. Rome numbers at arrows indicate the dispersion branch as indicated in Fig.31 a,b.

The PL angle diagrams, $I_\lambda(\theta)$, of a 2L-LB NCF obtained at wavelengths of 510, 550 and 590 nm are shown in Fig.6 together with corresponding transmission diagrams $T_\lambda(\theta)$. The transmission diagrams show the minima superimposed on a smooth background. The angular width of these minimum is less than $\pm 10^o$ with respect to the mid-gap direction. Comparison of emission and transmission diagrams reveals that the PL intensity peaks along the direction of the transmission minimum **[**89**]**. This observation correlates with the observation of the relative PL maxima at transmission minima (Fig.32 a,b). It is worth noting that $I_\lambda(\theta)$ does not follow the Lambert diagram $I_\lambda \propto \cos\theta$ (Fig.33c, 34a). To quantify the radiation power emitted by the NCF, we calculated the total area under the angle diagram $S^{60}_\lambda = \int_{\Delta\theta} I_\lambda(\theta) d\theta$, where the angle interval $\Delta\theta = 60^o$ (Fig.33c, 34a). Assuming the even azimuth distribution of the emission intensity and taking into account that the emission intensity becomes sufficiently low at $\theta \ge 60^o$, the S^{60}_λ is proportional to the power radiated at a given wavelength. Integration of the S^{60}_λ over the studied spectral range estimates the total emitted flux.

In order to characterize the effect of PhC coating upon the emission directionality, the S^{60}_λ area was normalized to that under the Lambert-like diagram, $S^L_\lambda = \int_{\Delta\theta} I(\lambda, \theta = 0^o)\cos\theta d\theta$,

where the intensity $I(\lambda,\theta=0^o)$ is taken from the experimental data and $\Delta\theta=60^o$. Deviation of the ratio $S_\lambda^{60}/S_\lambda^L$ spectrum of NCF-LB from that of bare NCF occurs in the PBG range: the width of the PL indicatrix is reduced by 14% at PBG wavelengths compared to that outside the PBG. Similar observations apply to samples with the 1L, 2L and 5L-thick crystals.

The quantity, S_λ^5, which is proportional to the emission flux propagating within the angular cone $\Delta\theta$ from 0° to 5° at a given wavelength along the film normal was calculated to map the emission diagram distortion in the angle-wavelength plane. S_λ^5 was then normalized to S_λ^{60} to obtain the fraction $S_\lambda^5/S_\lambda^{60}$. The spectrum of $S_\lambda^5/S_\lambda^{60}$ shows that the spectral band of enhanced emission is centred at 555 nm as a counterpart of the transmission minimum (Fig.34b). In contrast, the $S_\lambda^5/S_\lambda^{60}$ fraction for the bare NCF increases monotonically across the same wavelength range.

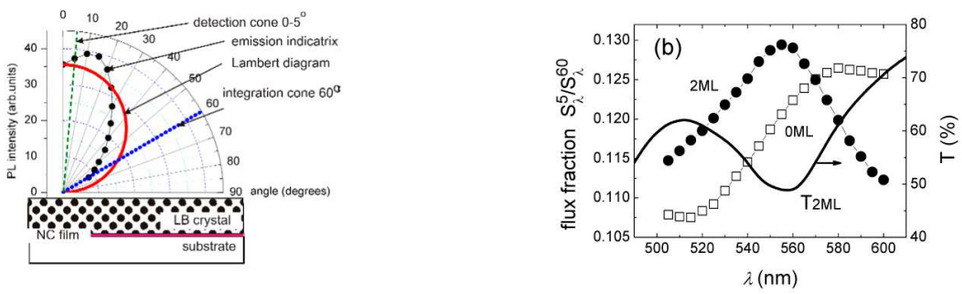

Fig. 34. (a) The definition of the 5°- and 60°-wide flux fractions – dashed and dotted lines, correspondingly. Dots show the PL indicatrix at $\lambda=590$ nm. Line is the Lambertian indicatrix. (b) Spectra of the emission flux fraction propagating along the film normal within a five degree wide cone for bare NCF (squares) and 2L-LB-NCF (circles) in comparison to the transmission spectrum of the 2L-LB-NCF (line).

By increasing the principal angle of the 5°-wide probe section the enhancement band follows the dispersion of the minimum of the far-field transmission spectra. This means that the radiation enhancement occurs in the direction of the transmission minimum, as it follows from comparison of Figs.35a and 32a. At higher angles, the enhancement becomes less pronounced in response to the decreasing attenuation in the corresponding transmission minimum. It is worth noting the resolution of other transmission minima is too poor to generate a corresponding flux maximum.

The diffraction in the 2D grating that is conveniently used in lightning devices for extraction of guided light [90,91]. For example, 1ML of SiO_2 spheres was able to diffract the beam of 4% bandwidth from the emission trapped in a glass plate between the light source and the monolayer of spheres [92]. The diffraction spectra were measured in order to exclude the diffraction outcoupling as the reason for the PL intensity increase. They were obtained keeping the sum of the incidence and diffraction angle constant $\theta+\alpha=76^o$. The dispersion of these resonances satisfies the expression

$$m\lambda_0=\Lambda(\pm\sin\theta\pm\sin\alpha) \tag{0.20}$$

or, in particular, $\lambda_0 = \Lambda(\sin\theta + \sin(76^o - \theta))$, where the grating period is $\Lambda = 456$ nm . This is the half of the period $a = \sqrt{3}D$ of the trigonal lattice for the wave vector of incident light propagating along the ΓK direction in the Brillouin zone of the 2D hexagonal lattice with the distance between centres of spheres of 526 nm. Such diffraction produces resonances at shorter wavelengths at $\theta \le 20^o$ compared to the eigenmodes of the 2D PhC (Fig.32d). Moreover, the PhC-induced band in the relative PL spectra (squares in Fig.35b) follows the dispersion branch I of transmission minima and does not satisfy the dispersion (0.20). Therefore, the enhanced PL band cannot be explained by the diffraction at the grating. This conclusion is also supported by comparison of the angle diagram of the intensity of the diffracted beam at $\lambda_0 = 550$ nm (crosses in Fig.33b) and the emission intensity diagram at the same wavelength. Hence, we can abandon the mechanism [93,94,95] assigning the increase of the PL intensity to diffractive outcoupling of the emission.

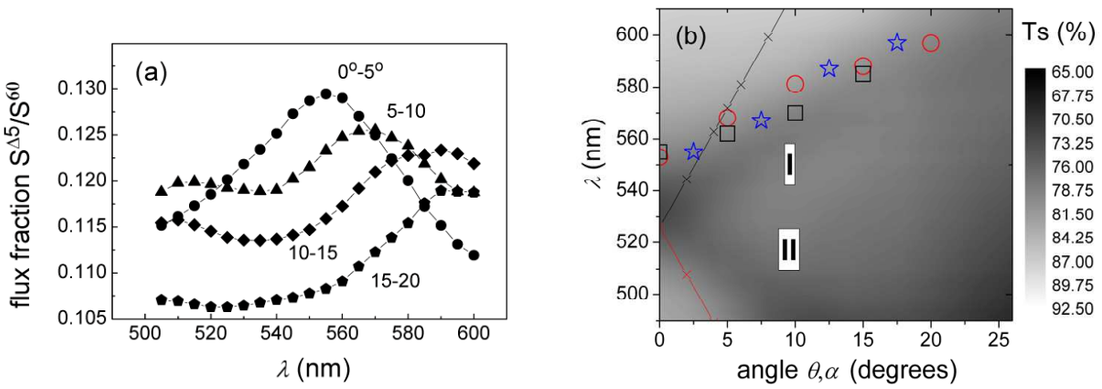

Fig. 35. (a) Spectra of the 5°-wide emission flux fractions propagating along different directions. (b) The transmission pattern of a 2L LB coating under s-polarized light. Squares and circles represent the dispersion of the enhancement band in the forward- and backward-measured relative PL spectra, respectively. Stars show the dispersion of peaks in radiation directionality spectra of panel (a). Dispersion of diffraction (0.20) is shown by crosses.

Another mechanism, the diffraction of the second order, assumes interaction of counter-propagating modes with the grating period that gives rise to the out-coupled beam with $\lambda_0 = 2n_{eff}\Lambda / m$, where $m > 1$. This beam propagates within a very narrow radiation cone along the grating normal [96,97]. However, this diffraction was also not observed.

More adequate explanation takes into account the PBG structure of a 2D lattice of dielectric spheres [98,99]. This model explains reasonably well the observed far-field transmission spectra and their angular dependence. Moreover, this theory predicts considerable broadening of the minima bandwidth due to light leakage to the substrate [100]. The spectral position of the first bandgap in such PhC corresponds to the sphere diameter and the next gap takes place at a wavelength, which is lower by a factor of 1.21. The observed minima at 548 and 444 nm for 1L LB film are in good agreement with this model. As was experimentally demonstrated, a 2D model remains valid for the description of the PBG structure at wavelengths $\lambda \approx D$ for LB colloidal multilayers [87].

Dips in transmission spectra of LB films appear due to light losses for the excitation of eigenmodes, which propagate in the LB film plane. At the PBG resonance, e.g. for $\theta \approx 0^o$ at $\Lambda/\lambda \approx 1$, the local field is enhanced by one (in the case of a PhC on a substrate [99,101]) or two orders of magnitude (for a PhC membrane [77]) due to large evanescent components of the EM field. The strong local field on a scale of the PhC lattice constant speeds up the radiative recombination rate as compared to that in bare NCF. The apparent independence of the magnitude of the emission enhancement upon the number of monolayers in multiple-layer LB films correlates with the surface-related nature of the observed effect.

With this picture in mind, the PL spectrum transformation can be explained as follows. In the case of the bare NCF, the emission is coupled to the substrate and free space. In the presence of an LB coating, the formation of "hot spots" of the local field at PBG wavelengths at PhC surface leads to a higher emission rate of NCs at these spots. Since the relative PL spectrum demonstrates a peak at PBG wavelengths, one can assume that the acceleration of the emission rate in "hot" spots prevails over the rate decrease at "cold" spots.

The PBG origin of the enhancement leads to the emission directionality in agreement with the angular dispersion of the PBG minimum. If NCs emit into eigenmodes of the PhC, then the outcoupling of this radiation is the reciprocal process with respect to the coupling of external radiation to PhC modes in a transmission experiment.

Interestingly, the emission indicatrix (Fig.33) in the studied case appears more sensitive to the PBG directionality compared to the PL spectra (Fig.30b), but the maximum in the directionality spectra agree the enhancement bands of the relative PL spectra (Fig.35b)

The strong argument in favour of the PBG-related enhancement mechanism is the correlation between the relative LB-NCF PL enhancement bands measured in the backward direction, for which the emission does not pass the LB crystal, and the minima in LB crystal transmission spectra (Fig.36). The structure of the forward and backward relative PL spectra and the dispersions of these bands are similar, i.e., enhancement reveals itself in opposite directions simultaneously, although less efficient in the backward direction. This property correlates the reciprocity of the LB-NCF sample transmission and the leakage character of guided modes in the LB-NCF sample. These observations point to the fact that the NCF forms an interacting unit with the LB PhC.

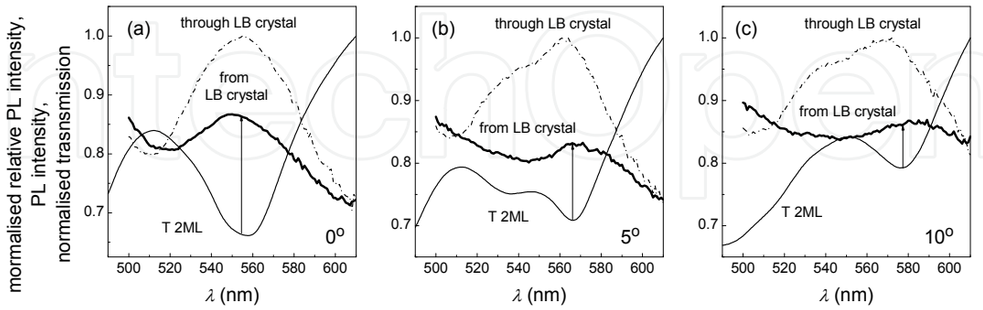

Fig. 36. Normalized angle-resolved transmission (thin solid line) and relative PL spectra at 0 (a), 5 (b) and 10° (c) of a 2L LB-NCF observed in the backward direction through the glass substrate (thick solid) and the forward direction through the LB crystal (dash-dotted lines). Arrows indicate the centres of transmission minima.

10. Summary

In this review we demonstrated different aspects of the PBG control on the emission of semiconductor nanocrystals that is coupled to optical modes of colloidal crystal-based thin film photonic crystals. We discussed (i) changes of the emission spectra and the emission directionality, (ii) methods used to recognise and estimate the emission modification, (iii) physical mechanisms behind the emission control and (iv) energy transfer between the nanocrystals and the carcass of photonic crystals. This basic information allows to estimate pros and contras of photonic crystal-integrated light sources and their prospects in the design of future lightning devices.

The described experiments were limited to the emission control in the spectral range of the lowest frequency directional bandgap, namely, the (111) bandgap in the opal crystals. The directional nature of this bandgap reduces dramatically the strength of the PBG effect because the light flow can escape the photonic crystal using remaining unblocked propagation directions. Preparing inverted opals from high refractive index dielectrics can at least partially lift up this problem due to smaller escape angle range.

Exploring the range of high order bandgaps is also in progress, but due to the nature of the photonic bandgap diagram, the (111) gap in opals is the only true one in terms of the absence of photon modes. All other high order bandgaps are, in fact, merely diffraction resonances with contribution of slow propagating modes. This uncertainty blurs up the physical mechanisms of emission modification. Obviously, in the case of inverted opals with an omnidirectional bandgap the physical nature of the emission control can reveal itself in a full extent, but such crystals were not yet reported for the visible for very fundamental reasons.

We did not also address any works related to optimisation of the NC-to-PhC interaction for following reasons. First, the PBG effect on emission of embedded sources strongly depends on the ordering of the crystal lattice. In this sense the photonic crystals prepared by nanolithography provide the precise control upon the light source positioning and overall lattice regularity, but at the cost of time-consuming and expensive technologies and small crystal volumes. Second, the design of light sources with specific functionality requires corresponding structuring of the photonic crystal, e.g., formation of resonators. Third, the optimisation usually exploits already established operation principles, but does not lead to new phenomena. Instead, we concentrated the attention on photonic crystals prepared by colloidal assembly because their combination with colloidal nanocrystals can benefit from inexpensive technology of both components, while preserves all possibilities for emission control offered by other realisations of photonic crystal-enhanced light sources. Overall, along the progress in improving the colloidal crystal ordering and methods of their structuring, this approach looks prospective for up-scaled production.

Acknowledgments

Authors gratefully acknowledge valuable contributions of their collaborators and colleagues N. Gaponik, A. Eychmueller, A.L. Rogach, M. Bardosova, C.M. Sotomayor Torres, D.N. Chigrin, V.G. Solovyev, R. Kian and R. Zentel.

11. References

1 Yin Y., A. P. Alivisatos, Colloidal nanocrystal synthesis and the organic–inorganic interface, *Nature*, **437** 664-670 (2005)

2 Rogach A. L., N. Gaponik, J. M. Lupton, C. Bertoni, D. E. Gallardo, S. Dunn, N. Li Pira, M. Paderi, P. Repetto, S.G. Romanov, C. O'Dwyer, C. M. Sotomayor Torres, A. Eychmüller, Light-Emitting Diodes with Semiconductor Nanocrystals, *Angewandte Chemie Int. Edition*, **47**, iss.35, 6538 – 6549 (2008)

3 Parcell E.M., Spontaneous emission probabilities at radio frequencies, *Phys.Rev.*, **69**, 681 (1946)

4 Bykov V. P., Spontaneous emission in a periodic structure, *Sov. Phys. JETP* **35**, 269-273 (1972).

5 Bykov V. P., Spontaneous emission from a medium with a band spectrum, *Sov. J. Quant. Electron*. **4**, 861-871 (1975).

6 John S., Strong localization of photons in certain disordered dielectric superlattices, *Phys.Rev. Lett.* **58**(23), 2486-2489 (1987).

7 Yablonovitch E., Inhibited Spontaneous Emission in Solid-State Physics and Electronics, *Phys. Rev. Lett.* **58**, 2059-2062 (1987).

8 Joannopoulos J. D., S. G. Johnson, J. N. Winn, R. D. Meade, Photonic Crystals: Molding the Flow of Light, 2nd Edition, Princeton University Press, Princeton and Oxford, 2008, 284p.

9 Sanders J. V. , Colour of Precious Opal, *Nature*, **2049**, 1151-1154 (1964).

10 Darragh P. J. , A. J. Gaskin, B. C. Terrell & J. V. Sanders, Origin of Precious Opal, *Nature*, **209**, 13-16 (1966).

11 Balakirev V.G., V.N.Bogomolov, V.V.Zhuravlev, Y.A.Kumzerov, V.P.Petranovskii, S.G.Romanov, LA.Samoilovich, Three-dimensional superlattices in the opals, *Crystallography Reports*, **38**, 348-353 (1993).

12 Lopez C., Material aspects of photonic crystals, *Advanced Mater.*, **15**, N20, 1679-1704 (2003).

13 Astratov V.N., V.N.Bogomolov, A.A. Kaplyanskii, A.V. Prokofiev, L.A. Samoilovich, S.M. Samoilovich, Yu.A. Vlasov, Optical Spectroscopy of Opal Matrices with CdS Embedded in its Pores: Quantum Confinement and Photonic Band Gap Effects, *Il Nuovo Cimento*, **17D**, 1349-1354 (1995).

14 Romanov S.G., A.V.Fokin, V.V.Tretiakov, V.Y.Butko, V.I.Alperovich, N.P.Johnson, C.M.Sotomayor Torres. Optical properties of ordered 3-dimensional arrays of structurally confined semiconductors. *J.Cryst.Growth*, **159**, 857-860 (1996).

15 Xia Y., B. Gates, Y. Yin, and Y. Lu, Monodispersed Colloidal Spheres: Old Materials with New Applications, *Adv. Mater.*, **12**, No. 10 693-713 (2000).

16 Gaponenko S.V., Bogomolov V.N., Kapitonov A.M., Prokofiev A.V., Eychmueller A., Rogach A.L., Electrons and photons in mesoscopic structures: Quantum dots in a photonic crystal, *JETP Letters,* **68**, №2, 142-147 (1998).

17 Lodahl P., A. F. van Driel, I. S. Nikolaev, A. Irman, K. Overgaag, D. Vanmaekelbergh, W. L. Vos, Controlling the dynamics of spontaneous emission from quantum dots by photonic crystals, *Nature*, **430** , 654-657 (2004).

18 Boedecker G., C. Henkel, Ch. Hermann, O. Hess, Spontaneous emission in photonic structures: Theory and simulation, pp.23-42 in "Photonic crystals – Advances in Design, Fabrication and Characterization", eds. K.Busch, S.Loelkes, R.B. Wehrspohn,. H.Foell, 354 p Wiley-VCH, Weinheim, 2004.
19 Sprik R., B. A. van Tiggelen, and A. Lagendijk, Optical emission in periodic dielectrics, *Europhys. Lett.* **35**, 265 (1996).
20 Vats N., S. John, K. Busch, Theory of fluorescence in photonic crystals, *Phys.Rev. A*, **65**, 043808-1-13 (2002).
21 John S.and J. Wang, Quantum optics of localized light in a photonic band gap, *Phys. Rev. B* **43**, 12 772-12789 (1991).
22 Vats N. and S. John, Non-Markovian quantum fluctuations and superradiance near a photonic band edge, *Phys. Rev. A* **58**, 4168-4185 (1998).
23 Busch K. and S. John, Photonic band gap formation in certain self-organizing systems, *Phys. Rev. E* **58**, 3896-3908 (1998).
24 Koenderink A.F.,L.Bechger,A.Lagendijk,W.L.Vos, An experimental study of strongly modified emission in inverse opal photonic crystals, *phys.stat.sol.*(a) **197** №.3,648–661 (2003).
25 Chabanov A. A., Y. Jun, and D. J. Norris, Avoiding Cracks in Self-Assembled Photonic Band Gap Crystals, *Appl. Phys. Lett***. 84**, 3573 (2004).
26 Khunsin W., G. Kocher, S. G. Romanov, C. M. Sotomayor Torres, Quantitative analysis of lattice ordering in thin film opal-based photonic crystals, *Adv. Funct. Mater.,* **18**, 2471-2479 (2008).
27 Romanov S. G., Specific features of polarization anisotropy in optical reflection and transmission of colloidal photonic crystals, *Phys. Solid State,* **52**, N 4, 844-854 (2010)
28 Rogach A. L., L. Katsikas, A. Kornowski, D. Su, A. Eychmueller, H. Weller, Synthesis and Characterization of Thiol-Stabilized CdTe Nanocrystals, *Ber. Bunsenges. Phys. Chem.* **100**, 1772-1778 (1996).
29 Romanov S. G., T. Maka, , C. M. Sotomayor Torres M. Müller, R. Zentel, D. Cassagne, J. Manzanares-Martinez and C. Jouanin, Diffraction of Light from Thin Film PMMA Opaline Photonic Crystals, *Phys. Rev. E*, **63**, 056603-1-5 (2001).
30 Nikolaev I. S., P. Lodahl, and W. L. Vos, Quantitative analysis of directional spontaneous emission spectra from light sources, in photonic crystals, *Phys.Rev. A* **71**, 053813-1-10 (2005).
31 Koenderink A. F. and W. L. Vos, Optical properties of real photonic crystals: anomalous diffuse transmission, *J. Opt. Soc. Am. B*, **22**, No. 5 1075-1084 (2005).
32 Romanov S. G., T. Maka, C. M. Sotomayor Torres, M. Müller, R. Zentel, Emission in an SnS_2 Inverted Opaline Photonic Crystal, *Appl. Phys. Lett*., **79**, 731-733 (2001).
33 Romanov S.G., A.V. Fokin, V.I. Alperovich, N.P. Johnson, R.M. De La Rue, The Effect of the Photonic Stop-Band upon the Photoluminescence of CdS in Opal, *Physica Status Solidi a*, **164**, 169-173 (1997).
34 Bogomolov V. N., S. V. Gaponenko, I. N. Germanenko, A. M. Kapitonov, E. P. Petrov, N. V. Gaponenko, A. V. Prokofiev, A. N. Ponyavina, N. I. Silvanovich, S. M. Samoilovich, Photonic band gap phenomenon and optical properties of artificial opals, *Phys.Rev. E*, **55**, 7619-7625 (1997).

35 Romanov S.G., M. A. Kaliteevski, C.M.Sotomayor Torres, J. Manzanares Martinez, D. Cassagne, J.P. Albert, A.V. Kavokin, V.V. Nikolaev, S.Brand, R.A. Abram, N. Gaponik, A. Eychmueller, A.L. Rogach, Stimulated emission due to light localization in the bandgap of disordered opals, *Phisica Status Solidi (c)*, **1**, 1522-1530 (2004).

36 Golub J. E., R. Eichmann, and P. Thomas, Dimensional crossover of exciton hopping relaxation in mesoscopic structures, *Europhys. Lett.* **47**(5), 628-631 (1999).

37 A.A. Kiselev, Hopping-induced energy relaxation with allowance for all possible versions of intercenter transitions, *Semiconductors* **32**(5), 504-508 (1998).

38 Baranovskii S. D., T. Faber, F. Hensel, and P. Thomas, On the Description of Hopping - Energy Relaxation and - Transport in Disordered Systems, *J. Non-Cryst. Solids* 198-**200**, 222-225 (1996).

39 Zegria G. G. and V. A. Kharchenko, New mechanism of Auger recombination of nonequilibrium current carriers in semiconductor heterostructures, *Sov.Phys.JETP*, **74**(1), 173-181 (1992).

40 Yeh P., Optical Waves in Layered Media, John Wiley&Sons, New York, 1998; ISBN 0-471-82866-1.

41 J Russell P.St., Optics of Floquet-Bloch waves in dielectric gratings, *Appl. Phys. B*, **39,** 231-246 (1986).

42 Kosaka H., T. Kawashima, A. Tomita, M. Notomi, T. Tamamura, T. Sato, S. Kawakami, Superprism phenomena in photonic crystals, *Phys. Rev. B*, 58 R10096-99 (1998).

43 Romanov S.G., D. N. Chigrin, T. Maka, M. Müller, R. Zentel, C. M. Sotomayor Torres, Directionality of light emission in three-dimensional opal-based photonic crystals, *Proc. SPIE Int. Soc. Opt. Eng*. **5825**, 160-172 (2005).

44 Romanov S. G., D.N. Chigrin, C. M. Sotomayor Torres, N. Gaponik, A. Eychmüller, A. L. Rogach, Emission Stimulation in a directional bandgap of a CdTe-loaded opal photonic crystal, *Phys.Rev.E.* **69**, 046606-1-4 (2004).

45 Johnson S.G., J.D. Joannopoulos, Block-iterative frequency-domain methods for Maxwell's equations in a plane-wave basis,*Optics Express*, **8** (2001) 173-190

46 Wiersma D.S. and A. Lagendijk, Light diffusion with gain and random lasers.*Phys. Rev.E.*, **54**(4), 4256-4265 (1996).

47 John S. and G. Pang, Theory of lasing in a multiple-scattering medium, *Phys. Rev.A.*, **54**(4), 3642-3652 (1996).

48 Vlasov Yu. A., M.A. Kaliteevski, and V.V. Nikolaev, Different regimes of light localization in a disordered photonic crystal, *Phys. Rev. B* , **60**(3), 1555-1562 (1999)

49 Kaliteevski M. A., J. Manzanares Martinez, D. Cassagne, and J. P. Albert, Disorder-induced modification of the transmission of light in a two-dimensional photonic crystal, *Phys.Rev.B.*, **66**, 113101-1-4 (2002).

50 Soest G. van, F. J. Poelwijk, R. Spirk, and A. Lagendijk, Dynamics of a random laser above threshold, *Phys. Rev. Lett.* **86**, 1522-1525 (2001).

51 D.N. Chigrin, Radiation pattern of a classical dipole in a photonic crystal: Photon focusing, *Phys. Rev.* E **70**, 056611-1-12 (2004).

52 Etchegoin P. and R. T. Phillips, Photon focusing, internal diffraction, and surface states in periodic dielectric structures, *Phys. Rev. B* **53**, 12674-12683 (1996).

53 Romanov S. G., D. N. Chigrin, V. G. Solovyev, T. Maka, N. Gaponik, A. Eychmüller, A. L. Rogach, and C. M. Sotomayor Torres, Light emission in a directional photonic bandgap, *Phys.stat.sol. (a)*, **197**, 662-672 (2003)

54 Ho K. M., C. T. Chan, and C. M. Soukoulis, Existence of a photonic gap in periodic dielectric structures, *Phys. Rev. Lett.* **65**, 3152-3155 (1990)

55 S. G. Romanov, U. Peschel, M. Bardosova, S. Essig, K. Busch, Suppression of the critical angle of diffraction in thin film colloidal photonic crystals, *Phys. Rev. B,* **82** (2010) in press.

56 Reynolds A., F. López-Tejeira, D. Cassagne, F. J. García-Vidal, C. Jouanin, and J. Sánchez-Dehesa, Spectral properties of opal-based photonic crystals having a SiO2 matrix*Phys. Rev. B*., **60**, 11422-11426 (1999).

57 Zhukov E. A., Y. Masumoto, H. M. Yates, M. E. Pemble, E.A. Muljarov, C. M. Sotomayor Torres and S. G. Romanov, Interface Interactions and the Photoluminescence from Asbestos-Templated InP Quantum Wires, *Microstructures and Superlattices*, **27**, No. 5/6, pp. 571-576 (2000).

58 Bardosova M., S.G. Romanov, C.M. Sotomayor Torres, N. Gaponik, A. Eychmueller, Y.A. Kumzerov, J. Bendall, Effect of template defects in radiative energy relaxation of CdTe nanocrystals in nanotubes of chrysotile asbestos, *Micro- and Meso-porous materials,* **107**, 212-218 (2007).

59 Mikhailovsky A.A., A.V. Malko, J.A. Hollingsworth, M.G. Bawendi, V.I. Klimov, Multiparticle interactions and stimulated emission in chemically synthesized quantum dots, *Appl.Phys.Lett.,* **80**, 2380 (2002).

60 Solovyev V. G., S. G. Romanov, C. M. Sotomayor Torres, M. Müller, R. Zentel, N. Gaponik, A. Eychmüller and A. L. Rogach. Modification of the spontaneous emission of CdTe nanocrystals in TiO_2 inverted opals, *J. Appl.Phys*., **94**, 1205-1210 (2003).

61 Astratov V.N., A.M. Adawi, S. Fricker, M.S. Skolnick, D.M. Whittaker, P.N. Pusey, Interplay of order and disorder in the optical properties of opal photonic crystals, *Phys. Rev. B*, **66**, 165215-1-13 (2002)

62 Stefanou N., V. Yannopapas, A. Modino, Heterostructures of photonic crystals: frequency bands and transmission coefficients, *Computer Physics Commun.* **113**, 49-77 (1998)

63 Romanov S. G., H. M. Yates, M. E. Pemble, R. M De La Rue, Opal-Based Photonic Crystal with Double Photonic Bandgap Structure, *J. Phys.: Cond. Matter* **12**, 8221-8229 (2000).

64 Istrate E., E. H. Sargent, Photonic crystal heterostructures and interfaces, *Rev. Modern Physics*, **78**, 455-481 (2006).

65 Gaponik N., A. Eychmüller, A.L. Rogach, V.G. Solovyev, C.M. Sotomayor Torres, S. G. Romanov, Structure-related optical properties of luminescent hetero-opals, *J. App. Phys*.**, 95**, 1029-1035 (2004).

66 Romanov S. G., N. Gaponik, A. Eychmüller, A.L. Rogach V. G. Solovyev, D.N. Chigrin and C. M. Sotomayor Torres, Light emitting opal-based photonic crystal heterojunctions, in "Photonic Crystals" eds. K. Busch, S.Lölkes, R. Wehrspohn, H. Föll, Wiley-VCH, Weinheim, ISBN-13: 978-3-527-40432-2, 132-152 (2004).

67 Romanov S.G., Optical characterization of opal photonic hetero-crystals, in "Frontiers of Multifunctional Integrated Nanosystems" eds. E. Buzaneva and P. Scharff, Kluwer Acad. Publ., ISBN978-1-4020-2171-8, 309-330 (2004).

68 Jiang P., G. N. Ostojic, R.Narat, D. M. Mittleman, V.L. Colvin, The Fabrication and Bandgap Engineering of Photonic Multilayers, *Adv. Mater.* **13**, No. 6, 389-393 (2001)
69 Decher G., Fuzzy Nanoassemblies: Toward Layered Polymeric Multicomposites. *Science*, **277** 1232-1237 (1997).
70 Rogach A. L., D. S. Koktysh, M. Harrison, N. A. Kotov, Layer-by-Layer Assembled Films of HgTe nanocrystals with Strong Infrared Emission, *Chem. Mater.*, **12**, 1526-1528 (2000).
71 Caruso F., Nanoengineering of Particle Surfaces. *Adv. Mater.*, **13**, 11-22 (2001).
72 Gaponik N., D. V. Talapin, A. L. Rogach, K. Hoppe, E. V. Shevchenko, A. Kornowski, A. Eychmüller, and H. Weller, Thiol-Capping of CdTe Nanocrystals: An Alternative to Organometallic Synthetic Routes, *J. Phys. Chem.* B **106**, 7177-7185 (2002).
73 Ding B., M. Bardosova, I. Povey, M. E. Pemble, and S.G. Romanov, Engineered Light Scattering in Colloidal Photonic Heterocrystals, *Adv. Funct. Mater.*, **20**, 853-860 (2010).
74 Ohtaka K., H. Miyazaki, T. Ueta, Near-field effect involving photonic bands, *Mat. Science and Engineering B*, **48** 153- 161 (I 997).
75 Fluck E., N. F. van Hulst, W. L. Vos, and L. Kuipers, Near-field optical investigation of three-dimensional photonic crystals, *Phys.Rev. E* **68**, 015601-1-4 (2003).
76 Koenderink A. F., M. Kafesaki, C. M. Soukoulis, V. Sandoghdar, Spontaneous emission rates of dipoles in photonic crystal membranes, *J.Opt.Soc.Am.*B, **23**, 1196-1206 (2006)
77 Inoue M., Enhancement of local field by a two-dimensional array of dielectric spheres placed on a substrate, *Phys.Rev.B*, **36**, 2852-2862 (1987).
78 Kurokawa Y., H. Miyazaki, Y. Jimba, Optical band structure and near-field intensity of a periodically arrayed monolayer of dielectric spheres on dielectric substrate of finite thickness, *Phys.Rev B* **69**, 155117-1-9 (2004).
79 Rigneault H., F.Lemarchand, A.Sentenac, H.Giovannini, Extraction of light from sources located inside waveguide grating structures, *Opt.Lett.*, **24**, 148-150 (1999).
80 Joyce W.B., R.Z. Bachrach, R.W.Dixon, D.A.Sealer, Geometrical properties of random particles and the extraction of photons from electroluminescent diodes, *J.Appl.Phys.*, **45**, 2229-2254 (1974).
81 Bermel P., C. Luo, L.Zeng, L. C. Kimerling, J. D. Joannopoulos, Improving thin-film crystalline silicon solar cell efficiencies with photonic crystals, *Optics Express*, **15**, №25, 16986-17000 (2007)
82 Boroditsky M., T. F. Krauss, R. Coccioli, R. Vrijen, R. Bhat, E. Yablonovitch, Light extraction from optically pumped light-emitting diode by thin-slab photonic crystals, *Appl. Phys.Lett.*, **75**, 1036-1039 (1999).
83 Romanov S.G., M. Bardosova, M. Pemble, C.M. Sotomayor Torres, N. Gaponik A. Eychmüller, Emission pattern of planar CdTe nanocrystal light source coated by two-dimensional Langmuir-Blodgett photonic crystal, *Materials Science and Engineering C,* **27**, 968-971 (2007) .
84 Gaponik N., A.L. Rogach, Aqueous synthesis of semiconductor nanocrystals in "Semiconductor Nanocrystal Quantum Dots. Synthesis, Assembly, Spectroscopy and Applications", Rogach, A. (Ed.), Springer, Wien, N ew York, 2008, 372 p., ISBN: 978-3-211-75235-7
85 Shavel V., N. Gaponik, A. Eychmüller. The Assembling of Semiconductor Nanocrystals, *Eur. J. Inorg. Chem.*, **18** 3613-3263, (2005).

86 Bardosova M., P. Hodge, V.Smatko R.H. Tredgold and D. Whitehead, A new method of forming synthetic opals, *Acta Phys. Slovaca*, **54**, 409-415 (2004).
87 Romanov S.G., M. Bardosova, M. Pemble, C.M. Sotomayor Torres, (2+1)-dimensional photonic crystals from Langmuir-Blodgett colloidal multilayers, *Applied Physics Letters,* **89**, 43105 (2006).
88 Romanov S.G., M. Bardosova, D.E. Whitehead, I. Povey, M. Pemble, C.M. Sotomayor Torres, Erasing diffraction orders – opal versus Langmuir-Blodgett colloidal crystals, *Applied Phys. Lett.,***90**,133101 (2007).
89 Romanov S.G., M. Bardosova, I.M. Povey, M. Pemble, C.M. Sotomayor Torres, N. Gaponik and A. Eychmüller, Modification of emission of CdTe nanocrystals by the local field of Langmuir-Blodgett colloidal photonic crystals , *J. Appl. Phys.* **104**, 103118 1-8 (2008).
90 Alferov Zh.I., V.M. Andreev, S.A.Gurevich, R.F.Kazarinov, V.R.Larionov, M.N. Mizerov, E.L.Portnoi, Semiconductor lasers with the light output through the diffraction grating on the surface of the waveguide layer, *IEEE J. Quant. Electronics*, **11**, 449-451 (1975).
91 Turnbull G. A., P. Andrew, M. J. Jory, W. L. Barnes, and I. D. W. Samuel, Relationship between photonic band structure and emission characteristics of a polymer distributed feedback laser, *Phys.Rev. B*, **64**, 125122-1-6 (2001).
92 Yamasaki T., K. Sumioka, and T. Tsutsui, *Appl.Phys.Lett,* Organic light-emitting device with an ordered monolayer of silica microspheres as a scattering medium, **76**, 1243-1245 (2000).
93 Dakks M.L., L.Khun, P.F.Heidrich, B.A. Scott, Grating Coupler For Efficient Excitation Of Optical Guided Waves In Thin Films, *Appl.Phys.Lett.*, **16**, 523-525 (1970).
94 Matterson B. J., J. M. Lupton, A.F. Safonov, M. G. Salt, Wi. L. Barnes, I. D. W. Samuel, Increased Efficiency and Controlled Light Output from a Microstructured Light-Emitting Diode, *Adv. Mater.* **13**, 123-127 (2001).
95 Ziebarth J. M., A. K. Saafir, S. Fan, M. D. McGehee, Extracting Light from Polymer Light-Emitting Diodes Using Stamped Bragg Gratings**,** *Adv. Funct. Materials,* **14**, 451 (2004).
96 Streifer W., D.R. Scifres, R.D. Burnham, Coupled wave analysis of DFB and DBR lasers *IEEE J. Quant. Electronics*, **13**, 134-141 (1977).
97 Kanskar M., P.Paddon, V.Pacradouni, R. Morin, A. Busch, J.F,Young, S.R. Johnson, J.MacKenzie, T. Tiedje, Observation of leaky slab modes in an air-bridged semiconductor waveguide with a two-dimensional photonic lattice, *Appl.Phys.Lett.*, **70**, 1438-1440 (1997).
98 Miyazaki H.T., H. Miyazaki, K.Ohtaka, T.Sato, Photonic band in two-dimensional lattices of micrometer-sized spheres mechanically arranged under a scanning electron microscope, *J. Appl. Phys.*, **87,** 7152-7159 (2000).
99 Miyazaki H.T., H. Miyazaki, K.Ohtaka, T.Sato, Photonic band in two-dimensional lattices of micrometer-sized spheres mechanically arranged under a scanning electron microscope, *J. Appl.Phys.*, **87,** 7152-7159 (2000).
100 Kurokawa Y., H.Miyazaki, Y.Jimba, Light scattering from a monolayer of periodically arrayed dielectric spheres on dielectric substrates, *Phys.Rev.B*, **65**, 201102-1-4 (2002).
101 Kurokawa Y., H. Miyazaki, Y. Jimba, Optical band structure and near-field intensity of a periodically arrayed monolayer of dielectric spheres on dielectric substrate of finite thickness, *Phys.Rev B* **69**, 155117-1-9 (2004).

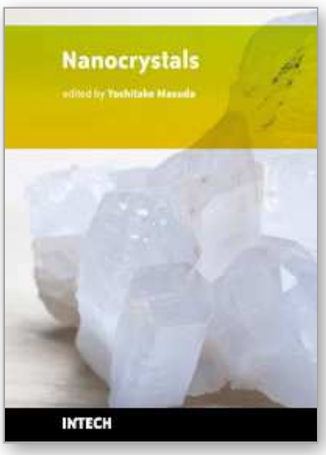

Nanocrystals

Edited by Yoshitake Masuda

ISBN 978-953-307-126-8
Hard cover, 326 pages
Publisher Sciyo
Published online 06, October, 2010
Published in print edition October, 2010

This book contains a number of latest research developments on nanocrystals. It is a promising new research area that has received a lot of attention in recent years. Here you will find interesting reports on cutting-edge science and technology related to synthesis, morphology control, self-assembly and application of nanocrystals. I hope that the book will lead to systematization of nanocrystal science, creation of new nanocrystal research field and further promotion of nanocrystal technology for the bright future of our children.

How to reference

In order to correctly reference this scholarly work, feel free to copy and paste the following:

Sergei Romanov and Ulf Peschel (2010). Emission of Semiconductor Nanocrystals in Photonic Crystal Environment, Nanocrystals, Yoshitake Masuda (Ed.), ISBN: 978-953-307-126-8, InTech, Available from: http://www.intechopen.com/books/nanocrystals/emission-of-semiconductor-nanocrystals-in-photonic-crystal-environment

INTECH
open science | open minds

InTech Europe
University Campus STeP Ri
Slavka Krautzeka 83/A
51000 Rijeka, Croatia
Phone: +385 (51) 770 447
Fax: +385 (51) 686 166
www.intechopen.com

InTech China
Unit 405, Office Block, Hotel Equatorial Shanghai
No.65, Yan An Road (West), Shanghai, 200040, China
中国上海市延安西路65号上海国际贵都大饭店办公楼405单元
Phone: +86-21-62489820
Fax: +86-21-62489821

IntechOpen